# The Inner Structure of ΛCDM Halos II: Halo Mass Profiles and LSB Rotation Curves

Eric Hayashi[1,6], Julio F. Navarro[1,6], Chris Power[2], Adrian R. Jenkins[2],
Carlos S. Frenk[2], Simon D. M. White[3], Volker Springel[3],
Joachim Stadel[4] and Thomas R. Quinn[5]

[1]*Department of Physics and Astronomy, University of Victoria, Victoria, BC, V8P 1A1, Canada*
[2] *Institute for Computational Cosmology, Department of Physics, University of Durham, South Road, Durham, DH1 3LE*
[3] *Max-Planck Institute for Astrophysics, Garching, Munich, D-85740, Germany*
[4] *Institute for Theoretical Physics, University of Zurich, Zurich CH-8057, Switzerland*
[5] *Department of Astronomy, University of Washington, Seattle, WA 98195, USA.*

## ABSTRACT

We use a set of high-resolution cosmological N-body simulations to investigate the inner mass profile of galaxy-sized cold dark matter (CDM) halos. These simulations extend the thorough numerical convergence study presented in Paper I of this series (Power et al. 2003), and demonstrate that the mass profile of CDM halos can be robustly estimated beyond a minimum converged radius of order $r_{\rm conv} \sim 1 \ h^{-1}$kpc in our highest resolution runs. The density profiles of simulated halos become progressively shallow from the virial radius inwards, and show no sign of approaching a well-defined power-law behaviour near the centre. At $r_{\rm conv}$, the logarithmic slope of the density profile is steeper than the asymptotic $\rho \propto r^{-1}$ expected from the formula proposed by Navarro, Frenk, and White (1996), but significantly shallower than the steeply divergent $\rho \propto r^{-1.5}$ cusp proposed by Moore et al. (1999). We perform a direct comparison of the spherically-averaged dark matter circular velocity ($V_c$) profiles with rotation curves of low surface brightness (LSB) galaxies from the samples of de Blok et al. (2001b), de Blok and Bosma (2002), and Swaters et al. (2003). Most (about two-thirds) LSB galaxies in this dataset are roughly consistent with CDM halo $V_c$ profiles. However, about one third of LSBs in these samples feature a sharp transition between the rising and flat part of the rotation curve that is not seen in the $V_c$ profiles of CDM halos. This discrepancy has been interpreted as excluding the presence of cusps, but we argue that it might simply reflect the difference between circular velocity and gas rotation speed likely to arise in gaseous disks embedded within realistic, triaxial CDM halos.

*Subject headings:* cosmology: theory – cosmology: dark matter – galaxies: formation – galaxies: spiral – galaxies: kinematics and dynamics

## 1. Introduction

The structure of dark matter halos and its relation to the cosmological context of their formation has been studied extensively over the past few decades. Early analytic calculations focused on the scale free nature of the gravitational accretion process and suggested that halo density profiles might be simple power laws (Gunn and Gott 1972; Fillmore and Goldreich 1984; Hoffman and Shaham 1985; White and Zaritsky 1992). Cosmological N-body simulations, however, failed to confirm these analytic expectations. Although power-laws with slopes close to those motivated by the theory were able to describe some parts of the halo

---

[6]Fellow of the Canadian Institute for Advanced Research and of the J.S.Guggenheim Memorial Foundation

density profiles, even early simulations found that significant deviations from a single power-law behaviour were present in most cases (Frenk et al. 1985, 1988; Quinn et al. 1986; Dubinski and Carlberg 1991; Crone et al. 1994). Further simulation work, indeed, concluded that power-law fits were inappropriate, and that, properly scaled, dark halos spanning a wide range in mass and size are well fit by a "universal" density profile (Navarro et al. 1995, 1996, 1997, hereafter NFW):

$$\rho_{\text{NFW}}(r) = \frac{\rho_s}{(r/r_s)(1 + r/r_s)^2}. \qquad (1)$$

One characteristic of this fitting formula is that the logarithmic slope, $\beta(r) = -d\log\rho/d\log r = (1 + 3y)/(1 + y)$ (where $y = r/r_s$ is the radius in units of a characteristic scale radius, $r_s$), increases monotonically from the centre outwards. The density profile steepens with increasing radius; it is shallower than isothermal inside $r_s$, and steeper than isothermal for $r > r_s$. Another important feature illustrated by this fitting formula is that the profiles are "cuspy"($\beta_0 = \beta(r = 0) > 0$): the dark matter density (but not the potential) diverges formally at the centre.

Subsequent work has generally confirmed these trends, but has also highlighted potentially important deviations from the NFW fitting formula. In particular, Fukushige and Makino (1997, 2001), as well as Moore and collaborators (Moore et al. 1998, 1999; Ghigna et al. 2000), have reported that NFW fits to their simulated halos (which had much higher mass and spatial resolution than the original NFW work) underestimate the dark matter density in the innermost regions ($r < r_s$). These authors proposed that the disagreement was indicative of inner density "cusps" steeper than the NFW profile and advocated a simple modification to the NFW formula so that $\beta_0 = 1.5$ (rather than 1.0).

The actual value of the asymptotic slope, $\beta_0$, is still being hotly debated in the literature (Jing et al. 1995; Klypin et al. 2001; Taylor and Navarro 2001; Navarro 2003; Power et al. 2003; Fukushige et al. 2003), but there is general consensus that CDM halos are indeed "cuspy". This has been recognized as an important result, since the rotation curves of many disk galaxies, and in particular of low surface brightness (LSB) systems, appear to indicate the presence of an extended region of con-

stant dark matter density: a dark matter "core" (Flores and Primack 1994; Moore 1994; Burkert 1995; Blais-Ouellette et al. 2001; de Blok et al. 2001a,b).

Unfortunately, rotation curve constraints are strongest just where numerical simulations are least reliable. Resolving CDM halos down to the kpc scales probed by the innermost points of observed rotation curves requires extremely high mass and force resolutions, as well as careful integration of particle orbits in the central, high density regions of halos. This poses a significant computational challenge that has been met in very few of the simulations published to date.

This difficulty has meant that rotation curves have usually been compared with extrapolations of the simulation data that rely heavily on the applicability and accuracy of fitting formulae such as the NFW profile to regions that may be severely compromised by numerical artifact. This practice does not allow for halo-to-halo variations, or for temporary departures from the "average" profile to be properly taken into account when trying to model the observational datasets.

Finally, the theoretical debate on the asymptotic central slope of the dark matter density profile, $\beta_0$, has led at times to unwarranted emphasis on the very inner region of the rotation curve datasets, rather than on an proper appraisal of the data over its full radial extent. For example, de Blok et al. (2001a,b) attempt to derive constraints on $\beta_0$ from the innermost few points of their rotation curves, and conclude that $\beta_0 \sim 0$ for most galaxies in their sample. However, their analysis focuses on the regions most severely affected by non-circular motions, seeing, misalignments and slit offsets, and other effects that limit the accuracy of circular velocity estimates based on long-slit spectra. It is perhaps not surprising, then, that other studies have disputed the conclusiveness of these findings.

Indeed, an independent analysis of data of similar quality by Swaters et al. (2003) (see also van den Bosch et al. 2000) concludes that "cuspy" dark matter halos with $\beta_0 \lesssim 1$ are actually consistent with their data. This disagreement is compounded by the results of the latest cosmological N-body simulations (Power et al. 2003, hereafter P03), which find scant evidence for a well defined value of $\beta_0$ in simulated CDM halos. Given these dif-

ficulties, focusing the theoretical or observational analysis on $\beta_0$ seems unwise.

In this paper, we improve upon previous work by comparing directly the actual results of the simulations with the full radial extent of the rotation curves of LSB galaxies. We present results from a set of seven galaxy-sized dark matter halos, each of which has been carefully simulated at various resolution levels in order to ascertain the numerical convergence of our results. This allows us to test rigorously the P03 convergence criteria, as well as to assess the cusp-core discrepancy through direct comparison between observation and simulations. A companion paper (Navarro et al. 2003) addresses the issue of universality of CDM halo structure using simulations that span a wide range of scales, from dwarf galaxies to galaxy clusters.

The outline of this paper is as follows. In §2 we introduce our set of simulations and summarize briefly our numerical methods. The seven galaxy-sized halos that form the core of our sample have been simulated at various resolutions, and we use them in §3 to investigate the robustness of the P03 numerical convergence criteria. The density profiles of these halos are presented and compared with previous work in §4. In §5 we compare the halo $V_c$ profiles with the LSB rotation curve datasets of de Blok et al. (2001b), de Blok and Bosma (2002), and Swaters et al. (2003). Our main conclusions and plans for future work are summarized in §6.

## 2. The Numerical Simulations

We have focused our analysis on seven galaxy-sized dark matter halos selected at random from two different cosmological N-body simulations of large periodic boxes with comoving size $L_{\rm box} = 32.5\,h^{-1}{\rm Mpc}$ and $35.325\,h^{-1}{\rm Mpc}$, respectively. Each of these "parent" simulations has $N_{\rm box} = 128^3$ particles, and adopts the currently favoured flat, low-density "concordance" $\Lambda$CDM world model, with $\Omega_0 = 0.3$, $\Omega_\Lambda = 0.7$, and either $h = 0.65$ (runs labelled G1, G2 and G3) or $h = 0.7$ (G4, G5, G6, and G7, see Table 1). The power spectrum in both simulations is normalized so that the linear rms amplitude of fluctuations on spheres of radius $8\,h^{-1}{\rm Mpc}$ is $\sigma_8 = 0.9$.

All halos (G1 to G7) have been re-simulated at three or four different mass resolution levels;

each level increases the number of particles in the halo by a factor of 8, so that the mass per particle has been varied by a factor 512 in runs G1-G3, and by a factor 64 in runs G4-G7 (see Table 1). All of these runs focus numerical resources on the Lagrangian region from where each system draws its mass, whilst approximating the tidal field of the whole box by combining distant particles into groups of particles whose mass increases with distance from the halo. This resimulation technique follows closely that described in detail in P03 and in Navarro et al. (2003), where the reader is referred to for full details. For completeness, we present here a brief account of the procedure.

Halos selected for resimulation are identified at $z = 0$ from the full list of halos with circular velocities in the range (150, 250) km s$^{-1}$ in the parent simulations. All particles within a sphere of radius $3\,r_{200}$[2] centred in each halo are then traced back to the initial redshift configuration ($z_i = 49$).

The region defined by these particles is typically fully contained within a box of size $L_{\rm sbox} \simeq 5\,h^{-1}{\rm Mpc}$, which is loaded with $N_{\rm sbox} = 32^3$, $64^3$, $128^3$, or $256^3$ particles. Particles in this new high-resolution region are perturbed with the same waves as in the parent simulation as well as with additional smaller scale waves up to the Nyquist frequency of the high resolution particle grid. Particles which do not end up within $3\,r_{200}$ of the selected halo at $z = 0$ are replaced by lower resolution particles which replicate the tidal field acting on the high resolution particles. This resampling includes some particles within the boundaries of the high resolution box, and therefore the high resolution region defines an asymmetrical "amoeba-shaped" three-dimensional volume surrounded by tidal particles whose mass increases with distance from this region.

A summary of the numerical parameters and halo properties is given in Table 1. This table also includes reference to 12 further runs, four of them corresponding to dwarf galaxy halos and eight of them to galaxy cluster-sized halos. These systems have been simulated only at the highest resolution ($N_{\rm sbox} = 256^3$), and therefore are not included

---

[2]We define the "virial radius", $r_{200}$, as the radius of a sphere of mean density 200 times the critical value for closure, $\rho_{\rm crit} = 3\,H^2/8\pi G$, where $H$ is Hubble's constant. We parameterize the present value of Hubble's constant $H$ by $H_0 = 100\,h$ km s$^{-1}$ kpc$^{-1}$

in our convergence analysis. These runs are discussed in detail in a companion paper (Navarro et al. 2003).

Some simulations were performed with a fixed number of timesteps for all particles using Stadel and Quinn's parallel N-body code `PKDGRAV` (Stadel 2001), while others used the N-body code `GADGET` (Springel et al. 2001). The `GADGET` runs allowed for individual timesteps for each particle assigned using either the `RhoSgAcc` or `EpsAcc` criterion (see P03 for full details). The halo labelled G1 in this paper is the same one selected for the numerical convergence study presented in P03. Although `PKDGRAV` also has individual timestepping capabilities, we have chosen not to take advantage of these for the simulations presented in this paper. We note that P03 finds only a modest computational gain due to multi-stepping schemes provided that the softening parameter is properly chosen.

The softening parameter (fixed in comoving coordinates) for each simulation (with the exception of G1/256$^3$, see P03) was chosen to match the "optimal" softening suggested by P03:

$$\epsilon_{\rm opt} = \frac{4\ r_{200}}{N_{200}^{1/2}}, \qquad (2)$$

where $N_{200}$ is the number of particles within $r_{200}$ at $z = 0$. This softening choice minimizes the number of timesteps required for convergence results by minimizing discreteness effects in the force calculations whilst ensuring adequate force resolution.

At $z = 0$, the mass within the virial radius, $M_{200}$, of our galaxy-sized halos ranges from $\sim 10^{12}\ h^{-1}M_\odot$ to $\sim 3 \times 10^{12}\ h^{-1}M_\odot$, corresponding to circular velocities, $V_{200} = (GM_{200}/r_{200})^{1/2}$, in the range $160\,{\rm km\,s^{-1}}$ to $230\,{\rm km\,s^{-1}}$.

## 3. Numerical Convergence

### 3.1. Criteria

P03 propose three different conditions that should be satisfied in order to ensure convergence in the circular velocity profile. According to these criteria, convergence to better than 10% in the spherically-averaged circular velocity, $V_c(r)$, is achieved at radii which satisfy the following conditions:

1. The local orbital timescale $t_{\rm circ}(r)$ is much

greater than the size of the timestep $\Delta t$:

$$\frac{t_{\rm circ}(r)}{t_{\rm circ}(r_{200})} \gtrsim 15 \left(\frac{\Delta t}{t_0}\right)^{5/6} \qquad (3)$$

where $t_0$ denotes the age of the universe, which is by definition of the order of the circular orbit timescale at the virial radius, $t_{\rm circ}(r_{200})$.

2. Accelerations do not exceed a characteristic acceleration, $a_\epsilon$, determined by $V_{200}$ and the softening length $\epsilon$:

$$a(r) = \frac{V_c^2(r)}{r} \lesssim a_\epsilon = 0.5\ \frac{V_{200}^2}{\epsilon} \qquad (4)$$

where $a(r)$ is the mean radial acceleration experienced by particles at a distance $r$ from the centre of the system, $a(r) = GM(r)/r^2 = V_c^2(r)/r$.

3. Enough particles are enclosed such that the local collisional relaxation timescale $t_{\rm relax}(r)$ is longer than the age of the universe[3]:

$$\frac{t_{\rm relax}(r)}{t_{\rm circ}(r_{200})} = \frac{\sqrt{200}}{8} \frac{N(r)}{\ln N(r)} \left(\frac{\overline{\rho}(r)}{\rho_{\rm crit}}\right)^{-1/2} \gtrsim 1 \qquad (5)$$

where $N(r)$ is the number of particles and $\overline{\rho}(r)$ is the mean density within radius $r$.

For "optimal" choices of the softening and timestep, as well as for the typical number of particles in our runs, we find that criterion (3) above is the strictest one.

The number of high-resolution particles thus effectively defines the "predicted" converged radius, $r_{\rm conv}$, beyond which, according to P03, circular velocities should be accurate to better than 10%. We emphasize that this accuracy criterion applies to the cumulative mass profile; convergence in properties such as local density estimates, $\rho(r)$, typically extends to radii significantly smaller than $r_{\rm conv}$.

---

[3]We adopt a slightly more conservative criterion than P03, who require $t_{\rm relax} \gtrsim 0.6\ t_{\rm circ}(r_{200})$.

### 3.2. Validating the Convergence Criteria

We assess the validity of the convergence criteria listed above by comparing the mass profile of the highest resolution run corresponding to each halo with those obtained at lower resolution. Figure 1 illustrates the procedure. From top to bottom, the three panels in this figure show, as a function of radius, the circular orbit timescale, the mean radial acceleration, and the relaxation timescale, respectively, for the four runs corresponding to halo G3. The small arrows at the bottom of each panel indicate the choice of gravitational softening for each run. The dotted curves in the top and middle panel show the best fit NFW profile to the converged region of the highest resolution $N_{\mathrm{sbox}} = 256^3$ run.

The "converged radius" corresponding to each criterion is determined by the intersection of the horizontal dashed lines in each panel with the "true" profile, which we shall take to be that of the highest resolution run (shown in solid black in Figure 1). Clearly, the strictest criterion is that imposed by the relaxation timescale (the dotted vertical lines in the lower panel show the converged radius corresponding to this criterion). This suggests, for example, that the lowest-resolution G3 run (with $N_{\mathrm{sbox}} = 32^3$, shown in solid blue), should start to deviate from the converged profiles roughly at $r \sim 0.1\, r_{200}$. Indeed, this appears to be the radius at which this profile starts to "peel off" from the highest resolution one, as shown in the top two panels of Figure 1. Increasing the number of high resolution particles by a factor of eight typically brings the converged radius inwards by a factor of $\sim 2.4$. For the medium-resolution run ($N_{\mathrm{sbox}} = 64^3$, shown in solid green), $r_{\mathrm{conv}}$ is predicted to be $\sim 0.04\, r_{200}$, which, again, coincides well with the radius inside which departures from the converged profile are apparent. Similarly, $r_{\mathrm{conv}} \sim 0.017\, r_{200}$ for the high-resolution ($N_{\mathrm{sbox}} = 128^3$) run (shown in red).

The density and circular velocity profiles corresponding to the four G3 runs are shown in Figure 2. Panels on the left show the profiles down to the radius that contains 50 particles, whereas those on the right show the profiles restricted to $r \gtrsim r_{\mathrm{conv}}$. Figure 2 illustrates two important results alluded to above: (i) both $\rho(r)$ and $V_c(r)$ converge well at $r \gtrsim r_{\mathrm{conv}}$, and (ii) convergence in

$\rho(r)$ extends to radii smaller than $r_{\mathrm{conv}}$. Indeed, the top-left panel shows that our choice of $r_{\mathrm{conv}}$ is rather conservative when applied to the density profile. Typically, densities are estimated to better than 10% down to $r \sim 0.6\, r_{\mathrm{conv}}$.

How general are these results? Figure 3 compares the minimum "converged" radius predicted by the P03 criteria , $r_{\mathrm{conv}}$, with $r_{10\%vc}$, the *actual* radius where circular velocities in the lower resolution runs deviate from convergence by more than 10%. In essentially all cases, $r_{\mathrm{conv}} \lesssim r_{10\%vc}$, indicating that the P03 criteria are appropriate, albeit at times somewhat conservative. We list our $r_{\mathrm{conv}}$ estimates for all runs in Table 1.

### 4. Halo Structure and Fitting Formulae

The dotted curves in Figure 2 show the best NFW fits to the density and circular velocity profile of the highest resolution run. The dashed lines correspond to the best fit adopting the modification to the NFW profile advocated by Moore et al. (1999),

$$\rho_{\mathrm{Moore}}(r) = \frac{\rho_M}{(r/r_M)^{1.5}(1 + (r/r_M)^{1.5})}. \qquad (6)$$

These fits are obtained by straightforward $\chi^2$ minimization in two parameters, $r_s$ or $r_M$, and the characteristic density $\rho_s$ or $\rho_M$. The profiles are calculated in bins of equal width in $\log r$, and the fits are performed over the radial range $r_{\mathrm{conv}} < r < r_{200}$. Equal weights are assigned to each radial bins because the statistical (Poisson) uncertainty in the determination of the mass within each bin is negligible (each bin contains thousands of particles) so uncertainties are completely dominated by systematic errors whose radial dependence is difficult to assess quantitatively.

The best fits to $\rho(r)$ and $V_c(r)$ shown in Figure 2 are obtained independently from each other. Values of the concentration parameter, $c_{\mathrm{NFW}} = r_{200}/r_s$, for the best fit NFW profiles are 6.4 and 5.3 for fits to the density and circular velocity profile, respectively; the Moore et al concentrations, $c_{\mathrm{Moore}} = r_{200}/r_M$, are 3.0 and 2.9 for the best fits to $\rho(r)$ and $V_c(r)$, respectively. Over the converged region, $r \gtrsim r_{\mathrm{conv}}$, both the NFW and Moore et al profiles appear to reproduce reasonably well the numerical simulation results. Indeed, no profile in the G3 runs deviates by more than

10% in $V_c$ or 30% in $\rho(r)$ from the best fits obtained with either eq. 1 or eq. 6. More substantial differences are expected only well inside $r_{\rm conv}$, but these regions are not reliably probed by the simulations.

This suggests that either the NFW or Moore et al profile may be used to describe the structure of $\Lambda$CDM halos outside $\sim 1\%$ of the virial radius, but also implies that one should be extremely wary of extrapolations inside this radius. One intriguing feature of Figure 2 is that the Moore et al formula appears to fit the G3 density profiles better than NFW but that $V_c$ profiles are somewhat better approximated by NFW (see also P03). This suggests that neither formula captures fully and accurately the radial dependence of the structure of $\Lambda$CDM halos.

### 4.1. The radial dependence of the logarithmic slope

This view is confirmed by the radial dependence of the logarithmic slope of the density profile $\beta(r) = -d\log\rho/d\log r$, which is shown in the top-left panel of Figure 4 for all the high-resolution runs, and compared with the predictions of the NFW (solid line) and Moore et al (dashed line) formulae.

Logarithmic slopes are calculated by numerical differentiation of the density profile, computed in radial bins of equal logarithmic width ($\Delta\log r/r_{200} \simeq 0.2$). The slope profiles in Figure 4 are normalized to $r_{-2}$, the radius where $\beta(r)$ takes the "isothermal" value of 2.[4] In this and all subsequent figures, profiles are shown only down to the minimum converged radius $r_{\rm conv}$. This corresponds typically to a radius $r_{\rm conv} \simeq 0.006 \; r_{200}$, or about 1-2 $h^{-1}$kpc for halos simulated at highest resolution (see Table 1).

The top left panel of Figure 4 shows that halos differ from the NFW and Moore et al formula in a number of ways:

- there is no obvious convergence to an asymptotic value of the logarithmic slope at the centre; the profile gets shallower all the way down to the innermost radius reliably resolved in our runs, $r_{\rm conv}$.

- the slope at $r_{\rm conv}$ is significantly shallower than the asymptotic value of $\beta_0 = 1.5$ advocated by Moore et al. (1999). The shallowest value measured at $r_{\rm conv}$ is $\beta \simeq 1$, and the average over all seven halos is $\beta \simeq 1.2$.

- Most halo profiles become shallower with radius more gradually than predicted by the NFW formula; at $r \sim 0.1 \; r_{-2}$ the average slope is $\sim -1.4$, whereas NFW would predict $\sim -1.18$. The NFW density profile turns over too sharply from $\rho \propto r^{-3}$ to $\rho \propto r^{-1}$ compared to the simulations.

In other words, the Moore et al profile appears to fit better the inner regions of the density profile of some $\Lambda$CDM halos (see bottom-left panel of Figure 4) *not* because the inner density cusp diverges as steeply as $\beta_0 = 1.5$, but rather because its logarithmic slope becomes shallower inwards less rapidly than NFW.

It is important to note as well that there is significant scatter from halo to halo, and that two of the seven density profiles are actually fit better by the NFW formula. Are these global deviations from a "universal" profile due to substructure? We have addressed this question by removing substructure from all halos and then recomputing the slopes. Substructure is removed by first computing the local density at the position of each particle, $\rho_i$, using a spline kernel similar to that used in Smoothed Particle Hydrodynamics (SPH) calculations[5]. Then, we remove all particles whose densities are more than 2 standard deviations above the spherically-averaged mean density at its location. (The mean and standard deviation are computed in bins of equal logarithmic width, $\Delta\log r/r_{200} \simeq 0.01$). The procedure is iterated until no further particles are removed. The remaining particles form a smoothly distributed system that appears devoid of substructure on all scales. We find that density profiles are smoother after the removal of substructure but that most of the variation in the overall shapes of the profiles remains. We conclude that the presence of substructure is not directly responsible for the observed scatter in the shape of halo density profiles.

---

[4]$r_{-2}$ is in this sense equivalent to the scale radius $r_s$ of the NFW profile.

[5]See `http://www-hpcc.astro.washington.edu/tools/smooth.html`

## 4.2. Comparison with Other Work

Are these conclusions consistent with previous work? To explore this issue, we have computed the logarithmic slope profile of three CDM halos run by Moore and collaborators. The halos we have re-analyzed are the Milky Way- and M31-like galaxy halos of the Local Group system from Moore et al. (1999) and the LORES version of the "Virgo" cluster halo from Ghigna et al. (2000). The $z \simeq 0.1$ output of the Local Group simulation was provided to us by the authors, whereas the Virgo cluster was re-run using initial conditions available from Moore's website[6]. The Virgo cluster run used the same N-body code as the original simulation (`PKDGRAV`) but was run with a fixed number of timesteps (12800). A run with 6400 timesteps was also carried out and no differences in the mass profiles were detected. The number of particles within the virial radius is $1.2 \times 10^6$, $1.7 \times 10^6$, and $5.0 \times 10^5$, for the Milky Way (MW), M31 and LORES Virgo cluster halos, respectively.

Figure 4 shows the logarithmic slope (upper right panel) and density (lower right panel) profiles corresponding to these halos, plotted down to the minimum converged radius $r_{\rm conv}$. No major differences between these simulations and ours are obvious from these panels. It is clear, for example, that at the innermost converged point, the slope of the density profile of the two Local Group halos is significantly shallower than $r^{-1.5}$, and shows no signs of having converged to a well defined power-law behaviour. There is some evidence for "convergence" to a steep cusp ($r^{-1.4}$) in the LORES Virgo cluster simulation but the dynamic range over which this behaviour is observed is rather limited. The Virgo cluster run thus appears slightly unusual when compared with other systems in our ensemble. Although our reanalysis confirms the conclusion of Moore et al. (1998, 1999) that this system appears to have a steeply divergent core, this does not seem to be a general feature of $\Lambda$CDM halos.

Our results thus lend support to the conclusions of Klypin et al. (2001), who argues that there is substantial scatter in the inner profiles of cold dark matter halos. Some are best described by the

NFW profile whereas others are better fit by the Moore et al formula, implying that studies based on a single halo might reach significantly biased conclusions.

Finally, we note that deviations from either fitting formula in the radial range resolved by the simulations, although significant, are small. Best NFW/Moore et al fits are typically accurate to better than $\sim 20\%$ in circular velocity and $\sim 40\%$ in density, respectively. We discuss in a companion paper (Navarro et al. 2003) the constraints placed by our simulations on extrapolations of these formulae to the inner regions as well as on the true asymptotic inner slope of $\Lambda$CDM halo density profiles.

## 5. Halo Circular Velocity Profiles and LSB Rotation Curves

As discussed in § 1, an important discrepancy between the structure of CDM halos and the mass distribution in disk galaxies inferred from rotation curves has been noted repeatedly in the literature over the past decade (Moore 1994; Flores and Primack 1994; Burkert 1995; McGaugh and de Blok 1998; Moore et al. 1999; van den Bosch et al. 2000; Côté et al. 2000; Blais-Ouellette et al. 2001; van den Bosch and Swaters 2001; Jimenez et al. 2003). In particular, the shape of the rotation curves of low surface brightness (LSB) galaxies has been identified as especially difficult to reconcile with the "cuspy" density profiles of CDM halos.

Given the small contribution of the baryonic component to the mass budget in these galaxies, the rotation curves of LSB disks are expected to trace rather cleanly the dark matter potential, making them ideal probes of the inner structure of dark matter halos in LSBs. Many of these galaxies are better fit by circular velocity curves arising from density profiles with a well defined constant density "core" rather than the cuspy ones inferred from simulations, a result that has prompted calls for a radical revision of the CDM paradigm on small scales (see e.g., Spergel and Steinhardt 2000)

It is important, however, to note a number of caveats that apply to the LSB rotation curve problem.

- Many of the early rotation curves where the disagreement was noted were unduly affected by beam smearing in the HI data

---

[6] `http://www.nbody.net`. We note that all of these runs were evolved in an $\Omega_0 = 1$ cosmogony, rather than the $\Lambda$CDM scenario we adopt in this paper.

(Swaters et al. 2000). For example, van den Bosch et al. (2000) argue that, once beam smearing is taken into account, essentially all HI LSB rotation curves are consistent with cuspy halo profiles. The observational situation has now improved substantially thanks to higher-resolution rotation curves obtained from long-slit $H_\alpha$ observations (see, e.g., McGaugh et al. 2001; de Blok et al. 2001a; Swaters et al. 2000, 2003). We shall restrict our analysis to these rotation curves in what follows.

- Strictly speaking, the observational disagreement is with the fitting formulae, rather than with the actual structure of simulated CDM halos. As noted in the previous section, there are systematic differences between them, so it is important to confirm that the disagreement persists when LSB rotation curves are contrasted directly with simulations.

- Finally, it must be emphasized that the rotation curve problem arises when comparing rotation speeds of gaseous disks to the spherically-averaged circular velocity profiles of dark matter halos. Given that CDM halos are expected to be significantly non-spherical (Barnes and Efstathiou 1987; Warren et al. 1992; Jing et al. 1995; Thomas et al. 1998; Jing and Suto 2002), some differences between the two are to be expected. It is therefore important to use the full 3D structure of CDM halos to make predictions regarding the rotation curves of gaseous disks that may be compared directly to observation. We shall neglect this complex issue in this paper, but plan to explore in detail the rotation curves of gaseous disks embedded in such asymmetric potentials in future papers of this series.

We may avoid many of these uncertainties by comparing directly the circular velocity profiles of our simulated halos with the observational data. This procedure has the advantage of retaining the diversity in the shapes of halo profiles that is often lost when adopting a simple analytic fitting formula. In addition, we consider circular velocity profiles only down to the innermost converged radius, thereby eliminating uncertainties about the reliability of the profile at very small radii.

We begin the analysis by emphasizing the importance of taking into account the changes in the central halo mass profile induced by accretion events. Indeed, these may trigger and sustain departures from the "average" profile that may be detectable in the rotation curves of embedded gaseous disks. We shall then describe a simple characterization of rotation curve shapes that may be applied to both observational and simulation data. This enables a direct and quantitative assessment of the "cusp" versus "core" problem as it applies to the most recent LSB datasets.

### 5.1. Evolution of the Inner Mass Profile

Systematic—and at times substantial—changes in the inner circular velocity profile are induced by accretion events during the assembly of the halo, even when such these events might contribute only a small fraction of mass to the inner regions. These transients may increase substantially the scatter in the shape of the $V_c$ profiles and they ought to be taken into account when comparing with observation.

This is illustrated in Figure 5, which shows the evolution of the mass and circular velocity profiles of halo G1. The top panel of this figure shows the evolution of the mass enclosed within 8, 10, 20 kpc (physical), and $r_{200}$, as a function of redshift. Although the mass inside 20 kpc increases by less than $\sim 25\%$ since $z = 1$, there are significant ($\sim 50 - 60\%$) fluctuations during this time caused by the tidal effects of orbiting substructure and accretion events. Most noticeable is a major merger at $z \simeq 0.7$, which affects the mass profile down to the innermost reliably resolved radius, $\simeq 2$ kpc.

The effect of these fluctuations on the circular velocity profile is shown in the bottom panel of Figure 5. Here we show the inner 20 kpc of the circular velocity profile before ($z = 1.1$), during ($z = 0.48$) and after ($z = 0$) a major accretion event. Substantial changes in the shape of the $V_c$ profile are evident as the halo responds to the infalling substructure. Note that the changes persist over timescales of order $\gtrsim 1$ Gyr, exceeding the circular orbital period at $r = 2$, 10, and 20 kpc ($\sim 0.13$, 0.34, and 0.58 Gyr, respectively). These

relatively long lasting changes thus would likely be reflected in the dynamics of a disk present at the centre of the halo.

## 5.2. LSB Rotation Curves

Could the evolutionary effects discussed above be responsible, at least in part, for the constant density cores inferred from the rotation curves of LSB and dwarf galaxies? Since it is nearly impossible to tailor a simulation to reproduce individual galaxies in detail, it is important to adopt a simple characterization of the rotation curves that allows for a statistical assessment of the disagreement between halo $V_c$ profiles and observation. We have thus adopted a three-parameter fitting formula commonly used in observational work to describe optical rotation curves (Courteau 1997):

$$V(r) = \frac{V_0}{(1 + x^\gamma)^{1/\gamma}}. \qquad (7)$$

Here $V_0$ is a velocity scale, $x = r_t/r$, where $r_t$ is a scale radius, and the dimensionless parameter $\gamma$ describes the overall shape of the curve. The larger the value of $\gamma$ the sharper the turnover from the "rising" to the "flat" region of the velocity curve. Eq. 7 is flexible enough to accommodate the shape of essentially all rotation curves in the samples we consider here. We note that this formula has three[7] free parameters, one more than the NFW profile.

We have applied this fitting formula to the HI/H$\alpha$ rotation curve datasets of de Blok et al. (2001b)[8], de Blok and Bosma (2002)[9], and Swaters et al. (2003)[10], hereafter B01, B02, and S03, respectively. Fits to the rotation curves and $V_c$ profiles are obtained through straightforward $\chi^2$-minimization, adopting the error estimates provided by the authors.

The B01 sample consists of 26 LSB galaxies, the B02 sample consists of 24 LSB galaxies, and the S03 sample contains 10 dwarf galaxies and 5

LSB galaxies. The smoothed rotation curves of B01 were derived by folding approaching and receding velocities about the centre of the galaxy (defined by the peak in the continuum emission) and using a spline-fitting procedure followed by rebinning to a bin width of 2". Error estimates were calculated as the quadratic sum of an observational error component caused by measurement uncertainties in the raw data points, and an additional error component due to differences between the approaching and receding velocities in the bin, as well as noncircular motions (defined as the difference between the mean velocity and the velocity of the spline fit). The rotation curve data provided by B02 are unsmoothed, with errors which include measurement, inclination, and asymmetry uncertainties. The rotation curves of S03 were derived by averaging receding and approaching velocity data in 2" bins; error estimates were defined by half the quadratic sum of the average error of points in the bin and half the difference between the maximum and minimum velocities in the bin.

The fit parameters for the combined set of 65 rotation curves are given in Table 2. In this table, $r_{\max}$ refers to the radius where the rotation curve reaches the maximum, $V_{\max}$. The outermost radius with reliable data is listed as $r_{\mathrm{outer}}$. Figure 6 shows a selected sample of rotation curves, together with the best fits obtained with eq. 7. The top, middle, and bottom rows include galaxies from the S03, B02, and B01 samples, respectively, arranged from left to right in order of increasing value of the shape parameter $\gamma$.

It is important to note that the rotation curves of B02 and S03 differ significantly from those of B01. The smoothing applied to the B01 dataset is clear in this figure, especially when compared with the less-processed B02 and S03 datasets. Because the B01 curves have been smoothed, the individual values quoted for the rotation speed are correlated, and the error estimates lack clear statistical meaning. This is confirmed by the extremely low values of the formal reduced $\chi^2$ obtained for the best fits with eq. 7 (see Table 2 and Figure 7): 16 out of 26 B01 galaxies have $\chi^2_{\mathrm{red}} < 0.1$ (and 5 have $\chi^2_{\mathrm{red}} < 0.01$), whereas all galaxies in S03's sample have $\chi^2_{\mathrm{red}} > 0.1$. This clearly advises against using $\chi^2$ as a goodness-of-fit measure intended to rule out a particular model.

---

[7]An additional factor of $(1 + x)^\beta$ was used by Courteau (1997) to improve fits to $\sim 10\%$ of the galaxies in his sample that exhibit a drop-off in the outer part of the rotation curve. For simplicity, we have not included this parameter in our fits.

[8]http://www.astro.umd.edu/~ssm/data

[9]ftp://cdsarc.u-strasbg.fr/cats/J/A+A/385/816

[10]http://www.robswork.net/data

### 5.3. LSB rotation curve shapes

The analysis procedures used by various authors induce significant differences in the rotation curves derived from the data, as illustrated by comparing the rotation curves of UGC 11557, and F568-3, the two galaxies common to the B01 and S03 samples, and UGC 4325, the only galaxy common to the B02 and S03 datasets. (Figure 8). The rotation curve of UGC 11557 (Figure 8, upper left panel) presented by B01 extends out to only $r \simeq 6$ kpc and rises with a nearly constant slope out to this radius. The best fit multi-parameter function has a scale radius $r_t = 14.1$ kpc, much greater than the outermost radius of the observations, $r_{\mathrm{outer}} = 6.2$ kpc, and a low value of $\gamma = 0.98$. The S03 rotation curve (Figure 8, upper right panel) for the same galaxy extends out to $r \simeq 10$ kpc and appears to level off in the last two data points. The scale radius of the fit to this curve is $r_t = 6$ kpc: well within the outermost radius of the observations $r_{\mathrm{outer}} = 10.4$ kpc, and different by a factor of two from that of the B01 curve. Although the value of the shape parameter $\gamma$ is actually lower for the S03 ($\gamma = 0.69$), it is clear that additional data points in the flat part of the curve, or smaller error bars on the last few points, would force the fit to higher values of $\gamma$. This would also result in fits with a much lower value of the asymptotic velocity $V_0$, which presently has a value much greater than the maximum velocity measured in either of the B01 or S03 rotation curves.

In the case of F568-3, B01's rotation curve (Figure 8, middle left panel) rises monotonically out to the last point and as a result, the multi-parameter function fits quite well ($\chi^2_{\mathrm{red}} = 0.031$). The S03 rotation curve extends out to the same outermost radius as the B01 curve and both curves are consistent with one another within the observational errors. Due to the different methods of estimating velocities, however, the B01 rotation curve is much smoother than that of S03. The S03 rotation curve (Figure 8, middle right panel) rises to a maximum at $r \simeq 6$ kpc then falls to $V_c \simeq 0.9 \ V_{\max}$ at the outermost radius $r_{\mathrm{outer}} = 11.2$ kpc. The fit to this curve is further complicated by a deviant data point at $r = 7$ kpc with a velocity, $V_c \simeq 0.7 \ V_{\max}$, much lower than that of neighbouring points. It is obvious that no simple fitting function can provide a good fit to this rotation curve. The best fit

multi-parameter function has a poor goodness-of-fit statistic $\chi^2_{\mathrm{red}} = 1.5$ and is characterized by an inordinately sharp turnover ($\gamma = 25.7$). We also note that the error bars in the B01 and S03 data are comparable in size ($\simeq \pm 8$ km s$^{-1}$) except near the radius of the discrepant point in the S01 curve, where error bars in the B01 data are twice as large ($\simeq \pm 16$ km s$^{-1}$). Clearly, the shape of the rotation curve as parameterized by fitting functions like the one given by eq. 7 is strongly influenced by the sensitivity of the observations, as well as by the method used to determine the rotation curve from the raw data.

Perhaps the most interesting case is the rotation curve of UGC 4325. The B02 and S03 versions of the rotation curve appear qualitatively different and are not consistent with one another within the error bars as presented. The B02 rotation curve rises monotonically out the last measured point, whereas the S03 curve flattens off sharply to a well-defined asymptotic value. Fits to the B02 and S03 rotation curves yield significantly different values for all three fitting parameters. The sharp turnover of the S03 curve results in a relatively large value of $\gamma = 3.67$ compared to $\gamma = 1.38$ for the fit to the B02 rotation curve. In addition, the asymptotic velocity $V_0$ of the B02 fit is more than twice that of the S03 fit. Of even greater concern is the maximum velocity one might infer for UGC 4325 from each version of the rotation curve. In the case of the B02 curve, the maximum velocity is undetermined but certainly appears to be greater than $V(r_{\mathrm{outer}}) \simeq 122$ km s$^{-1}$ since the curve is still rising at the outermost data point. According to the S03 curve, however, the maximum velocity is robustly determined, equal to the asymptotic velocity of the fit, $V_0 \simeq 94$ km s$^{-1}$. The maximum velocity one infers for UGC 4352 therefore differs by at least 30% depending on which rotation curve is used. This may have important consequences for the calculation of scaling parameters such as the central densities of galaxies, a point we return to in §5.6.

The spread in the best-fit parameters listed in the panels of Figure 8 is again a sobering reminder that a fair amount of non-trivial processing is involved when deriving rotation curves from raw data. Clearly, the disagreement between authors is somewhat worrying, and it limits the general applicability of conclusions inferred from individ-

ual galaxy studies. In spite of this, there appears to be broad statistical consistency between the rotation curve parameters derived by B01, B02 and S03. This is illustrated in the top panel of Figure 9, where we show the distribution of best-fit $\gamma$ values obtained for each sample. Each histogram in this figure is normalized to the total number of systems in each sample for ease of comparison. All three rotation curve datasets are broadly consistent with each other; in each case most ($70\% \pm 5\%$) LSB rotation curves are characterized by a value of $\gamma < 2$. These are typically gently-rising curves which turn over gradually as they approach the maximum asymptotic rotation speed, as shown, for example, by F574-1, and UGC 11454 in Figure 6. A significant ($\simeq 30\%$) number of 'outlier' galaxies with $\gamma \gtrsim 2.5$, however, populate the tail of the combined B01+B02+S03 distribution (see bottom panel of Figure 9). These are galaxies whose rotation curves feature a much "sharper" transition from the rising to flat part, as shown, for example, by F563-V2 and UGC 11748 in Figure 6.

## 5.4. Halo circular velocity profile shapes

The bottom panel of Figure 9 shows the $\gamma$ distribution obtained by fitting eq. 7 to the $V_c$ profile of all dwarf and galaxy-sized halos. In order to consider the various dynamical instances of a halo, we have included in the analysis about 20 different outputs for each system, spanning the redshift range $1 \lesssim z \leq 0$, giving a total of 266 halo profiles. We calculated the $V_c$ profile at each redshift in bins 1 kpc (physical) in width for the galaxy halos and 0.2 kpc (physical) in width for the dwarf halos, starting at the innermost reliably resolved radius $r_{\mathrm{conv}}$. The $V_c$ profiles were fit out to $r = 20$ kpc (physical) for the galaxy halos and $r = 8$ kpc (physical) for the dwarf halos, although we note that the fitting parameters are fairly insensitive to the region fitted provided that the curvature of the profile is well resolved. Since no formal error bars exist for the halo profiles (Poisson errors are negligible for the numbers of particles in these halos), we assign a uniform error of $\pm 1$ km s$^{-1}$ to all points.

The bottom panel of Figure 9 shows the distribution of $\gamma$ values obtained for the halos, after convolution with the typical uncertainty in $\gamma$ derived from fits to the observed rotation curves (an asymmetric Gaussian with $\sigma_{\gamma+} = 1.0$, $\sigma_{\gamma-} = 0.5$). The $\gamma$ distribution of all galaxy and dwarf halos, that of the dwarf halos only, and that of the combined B01, B02 and S03 sample are shown as the green, red and open histograms, respectively. The green and red histograms are normalized to the total number of halos, and the open histogram is normalized to the total number of galaxies in the combined observational dataset. As shown in Figure 9, the convolved halo $\gamma$ distribution peaks at $\gamma \simeq 0.6$, and has a dispersion of order $\sim 0.6$. For illustration, the three G1 $V_c$ profiles shown in the bottom panel of Figure 5 have $\gamma = 0.73$, 0.65, and 0.48 at $z = 1.1$, 0.48, and 0, respectively. There is no significant difference between the galaxy and dwarf halo $\gamma$ distributions.

## 5.5. Comparison

How does the distribution of rotation curve shapes compare with that of halo circular velocity profiles? The bottom panel of Figure 9 shows that, although there is significant overlap between the two distributions at values of $\gamma \lesssim 2$, most LSBs cluster around $\gamma \simeq 1.2$ compared to $\gamma \simeq 0.6$ for the halos. We note, however, that the contribution of a baryonic component has not been taken into account in our analysis of the simulated halo $V_c$ profiles. In order to investigate the effect of a baryonic disk on the shape of the $V_c$ profile, we construct an analytic mass model comprised of an NFW halo and an exponential disk. We use the prescription of Mo et al. (1998) to determine the scale length of the disk, $R_d$, as a function of the concentration, $c$, and spin parameter, $\lambda$, of the NFW halo, and the mass, $m_d$, and angular momentum, $j_d$, of the disk (expressed as fractions of the halo mass and angular momentum, respectively). Fitting eq. 7 to the inner 20 kpc of the resulting $V_c$ profiles, we find that the best fit $\gamma$ value changes from $\gamma = 0.72$ for an NFW halo with $c = 10$ and $r_{200} = 200\ h^{-1}$kpc, to $\gamma = 0.92\ (1.26)$ with the addition of a disk with $m_d = j_d = 0.05\ (0.1)$ assuming $\lambda = 0.1$, as expected for LSB disks.

We therefore conclude that the presence of the disk might be responsible for a significant sift in the peak of the $\gamma$ distribution.

This suggests that the shape of most LSB rotation curves might actually be consistent with the circular velocity profiles of $\Lambda$CDM halos. The major difference in the two distributions comes

from considering the outliers; in particular, systems with $\gamma \gtrsim 2.5$. Almost 1 in 3 LSBs is an outlier according to this definition, but such high values of $\gamma$ are rare amongst halos: fewer than 1 in 40 halos have $\gamma > 2.5$, and fewer than 1 in 100 have $\gamma > 3$. The "cusp vs. core" discrepancy alluded to above appears confined to less than a third of LSBs; those with sharp ($\gamma \gtrsim 2.5$) turnovers in their rotation curves.

We highlight the disagreement in Figure 10, where we show the $V_c$ profiles of all halos at $z \leq 1$ alongside two rotation curves; one with $\gamma \sim 1$ and another with a relatively high $\gamma \sim 5$. In order to concentrate on the *shape* of the rotation curve rather than on the physical scaling parameters, profiles have been scaled in this plot to the radius where the logarithmic slope of the fit to the rotation curve is equal to $d \log V / d \log r = 0.3$. We shall refer to this radius and its corresponding velocity as $r_{0.3}$ and $V_{0.3}$, respectively. These parameters are easily retrieved from the fits with eq. 7, and are given by: $r_{0.3} = (7/3)^{-1/\gamma} r_t$ and $V_{0.3} = (10/7)^{-1/\gamma} V_0$.

The scaled halo profiles are described reasonably well, on average, by the NFW profile, shown as the dashed curve in Figure 10, as is that of F571-8 ($\gamma = 0.83$). The shape of the rotation curve of F568-3 ($\gamma = 5.4$), on the other hand, is clearly inconsistent with the halo profiles. Better (albeit not perfect) fits to galaxies with $\gamma \gtrsim 2.5$ may be obtained using the circular velocity curve of a system with a constant density core, as shown by the pseudo-isothermal[11] model indicated by the dot-dashed curve in Figure 10.

### 5.6. The concentration of LSB halos

The discussion of the preceding section focused on the *shape* of the rotation curves and halo $V_c$ profiles. We now turn our attention to the physical parameters of the fits, in order to address claims that LSB galaxies are surrounded by halos of much lower concentration than expected in the $\Lambda$CDM scenario (McGaugh and de Blok 1998; de Blok et al. 2001b). We emphasize again that it is important to characterize both the observa-

tional data and the simulations in a way that is as independent as possible from fitting formulae or extrapolation. Alam et al. (2002) recently proposed a simple and useful dimensionless measure of mass concentration that satisfies these criteria,

$$\Delta_{V/2} \equiv \frac{\overline{\rho}(r_{V/2})}{\rho_{\rm crit}}. \qquad (8)$$

$\Delta_{V/2}$ measures the mean density contrast (relative to the critical density for closure) within the radius at which the rotation speed drops to one half of its maximum value, $V_{\rm max}$. In practice, we estimate $\bar{\rho}(r)$ by $3 V_c^2(r)/4\pi G r^2$, a quantity that is easily measured both in galaxies with rotation curve data (and well defined $V_{\rm max}$) and in simulated halos.

The top panel of Figure 11 shows $\Delta_{V/2}$ as a function of $V_{\rm max}$ for all galaxies in the B01, B02, and S03 samples (open symbols), together with the galaxy halos in our sample (filled circles). Filled triangles and squares correspond to simulated dwarf galaxy and cluster halos, respectively (see § 2).

The solid curve corresponds to the predictions of the Eke et al. (2001) halo concentration model for NFW halos in the $\Lambda$CDM cosmology we have assumed for our simulations. The dashed curves show the predictions of the Bullock et al. (2001) concentration model, together with the 1-$\sigma$ halo-to-halo scatter predicted by their model. Figure 11 shows that the simulations are in rough agreement with both models; the Bullock et al. (2001) model reproduces the simulations slightly better on the scales of dwarf halos, whilst the ENS model does better on the scale of clusters.

Figure 11 also shows that, on average, the concentration of $\Lambda$CDM is roughly comparable to those of LSBs in the samples we considered, although the scatter appears much larger than either obtained in the simulations or expected from the analytic model of Bullock et al. (2001). This result is reminiscent of our findings regarding the distribution of rotation curve parameter $\gamma$ (see Figure 9): CDM halos appear consistent with the *bulk* of LSBs but are at odds with the most deviant systems in the sample.

In order to investigate the effect of observational uncertainties on this parameter we examine the values of $\Delta_{V/2}$ calculated for UGC 4325.

---

[11]The density profile of this widely used approximation to the non-singular isothermal sphere is given by $\rho_{\rm iso}(r) = \rho_0/(1 + (r/r_c)^2)$, where $r_c$ is the core radius and $\rho_0$ is the characteristic density of the core.

As discussed in §5.2, the maximum velocities measured by B02 and S03 differ by 30% for this galaxy. The corresponding values of $\Delta_{V/2}$ are shown as the open triangle (B02) and open square (S03) points in the top panel of Figure 11. Surprisingly, we find that the inferred halo central densities are very similar for the two versions of the rotation curve. Because $\Delta_{V/2}$ depends only on the ratio between $V_{\max}$ and the radius $R_{V/2}$, two curves with very different maximum velocities can give the same value of $\Delta_{V/2}$ provided that the rising parts of the curves have the same slope. The halo central densities one infers from the B02 and S03 versions of the rotation curve for UGC 4325 are within 20% of one another despite a 30% difference in $V_{\max}$ between the two curves. This level of uncertainty in $\Delta_{V/2}$ is negligible considering that the halo-to-halo scatter in the simulations and model predictions spans a factor of 6 at a given $V_{\max}$.

Although the effect of observational uncertainties may be relatively unimportant in the case of UGC 4325, we nonetheless attempt to reduce the scatter in the $\Delta_{V/2}$ by culling from the sample all galaxies whose rotation curves are still rising at the outermost radius probed by the data. The bottom panel of Figure 11 shows the central densities inferred from rotation curves with $d \log V / d \log r(r_{\mathrm{outer}}) < 0.1$. We find that this reduced sample retains much of the original scatter, and many points lie both above and below the model predictions at a given value of $V_{\max}$.

Our results thus agree with those of Zentner and Bullock (2002), who have argued that the large number of low-concentration galaxies in LSB samples calls for substantial revision of the "concordance" $\Lambda$CDM scenario, such as tilted power spectra, running spectral index, or perhaps a lower $\sigma_8$. However, it appears unlikely that any such modification to the $\Lambda$CDM scenario would result in the larger variety of rotation curve shapes and concentrations apparently demanded by the LSB datasets. It is unclear at this point how to reduce the disagreement, but any resolution to the puzzle must explain why so many LSBs are actually in good agreement with $\Lambda$CDM halos and why the disagreement is confined to a minority of systems. The possibility remains that some complex astrophysical process not yet considered in the models might actually be behind the discrepancy and that no radical modification to the $\Lambda$CDM paradigm is called for.

## 6. Conclusions

We present results from a set of high resolution cosmological simulations of dark matter halos formed in a $\Lambda$CDM cosmogony. Seven Milky Way-sized galaxy halos were simulated at various mass, time, and spatial resolutions, enabling us to investigate the convergence properties of cosmological N-body simulations. We have examined the internal structure of the highest resolution realization of each halo, with particular emphasis on the logarithmic slope of the inner density profile. Finally, we have compared the circular velocity profiles of these halos with the rotation curves of a large sample of dwarf and LSB galaxies.

Our main conclusions may be summarized as follows.

- The convergence criteria proposed by Power et al. (2003) are robust, and provide a conservative estimate of the minimum radius at which the mass profile of simulated halos can be reliably predicted. According to these criteria, the highest resolution galaxy halos we have simulated (which contain 2-4 million particles within the virial radius) are reliably resolved down to $r_{\mathrm{conv}} \simeq 1 \ h^{-1}\mathrm{kpc}$.

- The slope of $\Lambda$CDM halo density profiles becomes progressively shallow all the way down to the minimum reliably resolved radius, without sign of converging to a a well-defined power law near the centre.

- In general, the slope changes with radius more gradually than predicted by the NFW formula, which leads some halos to be better described by profiles with steeper cusps, such as the modification to the NFW formula proposed by Moore et al (1999). There is, however, significant variation from halo to halo in the radial dependence of the slope. Some systems are better fit by the NFW profile, and others by the Moore et al formula. At $r_{\mathrm{conv}}$, however, the density profiles are significantly shallower than $r^{-1.5}$, the asymptotic value advocated by Moore et al. (1999).

- A comparison of the circular velocity profiles of ΛCDM halos with rotation curves of dwarf and LSB galaxies indicates that the shapes of most ($\simeq 70\%$) LSB rotation curves are consistent with those of simulated halo $V_c$ profiles. The remaining $\simeq 30\%$ feature a sharp turnover from the rising to the flat part of the curve which is not consistent with the structure of simulated halos.

- The concentration of dwarf and galaxy-sized halos simulated in the "concordance" ΛCDM cosmogony is in reasonable agreement with the characteristic central density inferred for most LSB galaxies from rotation curve data. However, as with the rotation curve shape, a significant number of LSBs have concentrations well below (and above) the expected range.

We conclude that the inner structure of ΛCDM halos is not manifestly inconsistent with the rotation curves of LSB galaxies, although they seem unable to reproduce the full variety of LSB rotation curve shapes and normalizations. This discrepancy may signal the need to revise some of the basic tenets of the ΛCDM scenario, but it might also taken to imply that the relation between gas rotation speeds and spherically-averaged halo circular velocities is more complex than assumed in simple analyses such as the one presented here.

CDM halos, for example, are known to be triaxial, which may lead gaseous disks to deviate systematically and significantly from simple coplanar circular orbits. Work is in progress to try and determine whether such asymmetries in the potential are able to account quantitatively for the "cusp vs core" discrepancy. Until this or other plausible astrophysical origin for the discrepancy is identified, the observed variety of LSB rotation curves and concentrations will remain a challenge that the theory must meet.

## REFERENCES

Alam, S. M. K., Bullock, J. S., and Weinberg, D. H.: 2002, *ApJ* **572**, 34

Barnes, J. and Efstathiou, G.: 1987, *ApJ* **319**, 575

Blais-Ouellette, S., Amram, P., and Carignan, C.: 2001, *AJ* **121**, 1952

Bullock, J. S., Kolatt, T. S., Sigad, Y., Somerville, R. S., Kravtsov, A. V., Klypin, A. A., Primack, J. R., and Dekel, A.: 2001, *MNRAS* **321**, 559

Burkert, A.: 1995, *ApJ* **447**, L25+

Côté, S., Carignan, C., and Freeman, K. C.: 2000, *AJ* **120**, 3027

Courteau, S.: 1997, *AJ* **114**, 2402

Crone, M. M., Evrard, A. E., and Richstone, D. O.: 1994, *ApJ* **434**, 402

de Blok, W. J. G. and Bosma, A.: 2002, *A&A* **385**, 816

de Blok, W. J. G., McGaugh, S. S., Bosma, A., and Rubin, V. C.: 2001a, *ApJ* **552**, L23

de Blok, W. J. G., McGaugh, S. S., and Rubin, V. C.: 2001b, *AJ* **122**, 2396

Dubinski, J. and Carlberg, R. G.: 1991, *ApJ* **378**, 496

Eke, V. R., Navarro, J. F., and Steinmetz, M.: 2001, *ApJ* **554**, 114

Fillmore, J. A. and Goldreich, P.: 1984, *ApJ* **281**, 1

Flores, R. A. and Primack, J. R.: 1994, *ApJ* **427**, L1

Frenk, C. S., White, S. D. M., Davis, M., and Efstathiou, G.: 1988, *ApJ* **327**, 507

Frenk, C. S., White, S. D. M., Efstathiou, G., and Davis, M.: 1985, *Nature* **317**, 595

Fukushige, T., Kawai, A., and Makino, J.: 2003, Preprint [astro-ph/0306203]

Fukushige, T. and Makino, J.: 1997, *ApJ* **477**, L9

Fukushige, T. and Makino, J.: 2001, *ApJ* **557**, 533

Ghigna, S., Moore, B., Governato, F., Lake, G., Quinn, T., and Stadel, J.: 2000, *ApJ* **544**, 616

Gunn, J. E. and Gott, J. R. I.: 1972, *ApJ* **176**, 1

Hoffman, Y. and Shaham, J.: 1985, *ApJ* **297**, 16

Jimenez, R., Verde, L., and Oh, S. P.: 2003, *MNRAS* **339**, 243

Jing, Y. P., Mo, H. J., Borner, G., and Fang, L. Z.: 1995, *MNRAS* **276**, 417

Jing, Y. P. and Suto, Y.: 2002, *ApJ* **574**, 538

Klypin, A., Kravtsov, A. V., Bullock, J. S., and Primack, J. R.: 2001, *ApJ* **554**, 903

McGaugh, S. S. and de Blok, W. J. G.: 1998, *ApJ* **499**, 41

McGaugh, S. S., Rubin, V. C., and de Blok, W. J. G.: 2001, *AJ* **122**, 2381 (M01)

Mo, H. J., Mao, S., and White, S. D. M.: 1998, *MNRAS* **295**, 319

Moore, B.: 1994, *Nature* **370**, 629

Moore, B., Ghigna, S., Governato, F., Lake, G., Quinn, T., Stadel, J., and Tozzi, P.: 1999, *ApJ* **524**, L19 (M99)

Moore, B., Governato, F., Quinn, T., Stadel, J., and Lake, G.: 1998, *ApJ* **499**, L5

Navarro, J. F.: 2003, in J. Makino and P.Hut (eds.), *Astrophysical SuperComputing using Particles*, IAU Symposium No. 208

Navarro, J. F., Frenk, C. S., and White, S. D. M.: 1995, *MNRAS* **275**, 720

Navarro, J. F., Frenk, C. S., and White, S. D. M.: 1996, *ApJ* **462**, 563 (NFW)

Navarro, J. F., Frenk, C. S., and White, S. D. M.: 1997, *ApJ* **490**, 493

Navarro, J. F., Hayashi, E., Power, C., Jenkins, A., Frenk, C., White, S. D. M., Springel, V., Stadel, J., and Quinn, T.: 2003, in preparation

Power, C., Navarro, J. F., Jenkins, A., Frenk, C. S., White, S. D. M., Springel, V., Stadel, J., and Quinn, T.: 2003, *MNRAS* **338**, 14 (P03)

Quinn, P. J., Salmon, J. K., and Zurek, W. H.: 1986, *Nature* **322**, 329

Spergel, D. N. and Steinhardt, P. J.: 2000, *Physical Review Letters* **84**, 3760

Springel, V., Yoshida, N., and White, S. D. M.: 2001, *New Astronomy* **6**, 79

Stadel, J. G.: 2001, *Ph.D. thesis*, University of Washington

Swaters, R. A., Madore, B. F., and Trewhella, M.: 2000, *ApJ* **531**, L107

Swaters, R. A., Madore, B. F., van den Bosch, F. C., and Balcells, M.: 2003, *ApJ* **583**, 732 (S03)

Taylor, J. E. and Navarro, J. F.: 2001, *ApJ* **563**, 483

Thomas, P. A., Colberg, J. M., Couchman, H. M. P., Efstathiou, G. P., Frenk, C. S., Jenkins, A. R., Nelson, A. H., Hutchings, R. M., Peacock, J. A., Pearce, F. R., and White, S. D. M.: 1998, *MNRAS* **296**, 1061

van den Bosch, F. C., Robertson, B. E., Dalcanton, J. J., and de Blok, W. J. G.: 2000, *AJ* **119**, 1579

van den Bosch, F. C. and Swaters, R. A.: 2001, *MNRAS* **325**, 1017

Warren, M. S., Quinn, P. J., Salmon, J. K., and Zurek, W. H.: 1992, *ApJ* **399**, 405

White, S. D. M. and Zaritsky, D.: 1992, *ApJ* **394**, 1

Zentner, A. R. and Bullock, J. S.: 2002, *Phys. Rev. D* **66**, 43003

TABLE 1

NUMERICAL AND PHYSICAL PROPERTIES OF SIMULATED HALOS

| Label | $R_{200}$ $h^{-1}$kpc | $M_{200}$ $h^{-1}M_\odot$ | $N_{200}$ | $\epsilon$ $h^{-1}$kpc | $N_{\Delta t}$ | Code | $r_{\rm conv}$ $h^{-1}$kpc |
|---|---|---|---|---|---|---|---|
| G1/32$^3$ | 202.1 | 191.8 | 5758 | 10 | 800 | PKDGRAV | 22.9 |
| G1/64$^3$ | 205.2 | 201.1 | 48318 | 2.5 | 1600 | PKDGRAV | 7.7 |
| G1/128$^3$ | 205.1 | 200.6 | 383560 | 1.25 | 3200 | PKDGRAV | 3.2 |
| G1/256$^3$ | 214.4 | 229.4 | 3447447 | 0.15625 | RhoSgAcc | GADGET | 1.4 |
| | | | | | | | |
| G2/32$^3$ | 231.4 | 288.1 | 8583 | 10 | 800 | PKDGRAV | 24.2 |
| G2/64$^3$ | 231.8 | 289.8 | 69088 | 3.5 | 1600 | PKDGRAV | 7.0 |
| G2/128$^3$ | 234.1 | 298.6 | 566456 | 1.25 | 3200 | PKDGRAV | 2.9 |
| G2/256$^3$ | 232.6 | 292.9 | 4523986 | 0.5 | 6400 | PKDGRAV | 1.3 |
| | | | | | | | |
| G3/32$^3$ | 218.7 | 243.1 | 5484 | 10 | 800 | PKDGRAV | 22.5 |
| G3/64$^3$ | 215.0 | 231.1 | 41719 | 3.5 | 1600 | PKDGRAV | 9.3 |
| G3/128$^3$ | 214.5 | 229.7 | 331314 | 1.25 | 3200 | PKDGRAV | 3.9 |
| G3/256$^3$ | 212.7 | 223.8 | 2661091 | 0.45 | 6400 | PKDGRAV | 1.7 |
| | | | | | | | |
| G4/64$^3$ | 164.9 | 104.4 | 53331 | 2.5 | 3200 | PKDGRAV | 5.7 |
| G4/128$^3$ | 165.4 | 105.3 | 432313 | 1 | 6400 | PKDGRAV | 2.4 |
| G4/256$^3$ | 164.0 | 102.6 | 3456221 | 0.3 | 12800 | PKDGRAV | 1.0 |
| | | | | | | | |
| G5/64$^3$ | 165.3 | 105.0 | 62066 | 3 | 800 | PKDGRAV | 5.7 |
| G5/128$^3$ | 165.7 | 105.8 | 496720 | 1 | 3200 | PKDGRAV | 2.3 |
| G5/256$^3$ | 165.0 | 104.5 | 3913956 | 0.35 | 6400 | PKDGRAV | 1.0 |
| | | | | | | | |
| G6/64$^3$ | 160.7 | 96.5 | 57008 | 3 | 800 | PKDGRAV | 6.0 |
| G6/128$^3$ | 163.2 | 101.1 | 474844 | 1 | 3200 | PKDGRAV | 2.5 |
| G6/256$^3$ | 162.5 | 99.9 | 3739913 | 0.35 | 6400 | PKDGRAV | 1.0 |
| | | | | | | | |
| G7/64$^3$ | 159.7 | 94.7 | 55947 | 3 | 800 | PKDGRAV | 5.8 |
| G7/128$^3$ | 160.9 | 96.9 | 454936 | 1 | 3200 | PKDGRAV | 2.4 |
| G7/256$^3$ | 160.3 | 95.8 | 3585676 | 0.35 | 6400 | PKDGRAV | 1.0 |
| | | | | | | | |
| D1 | 32.3 | 0.8 | 784980 | 0.0625 | EpsAcc | GADGET | 0.3 |
| D2 | 34.1 | 0.9 | 778097 | 0.0625 | EpsAcc | GADGET | 0.4 |
| D3 | 32.3 | 0.8 | 946421 | 0.0625 | EpsAcc | GADGET | 0.3 |
| D4 | 34.7 | 1.0 | 1002098 | 0.0625 | EpsAcc | GADGET | 0.3 |
| | | | | | | | |
| C1 | 1502.1 | 78842.4 | 1565576 | 5.0 | EpsAcc | GADGET | 16.8 |
| C2 | 1468.1 | 73618.2 | 1461017 | 5.0 | EpsAcc | GADGET | 16.9 |
| C3 | 1300.6 | 51179.5 | 1011918 | 5.0 | EpsAcc | GADGET | 16.1 |

TABLE 1—*Continued*

| Label | $R_{200}$ $h^{-1}$kpc | $M_{200}$ $h^{-1}M_\odot$ | $N_{200}$ | $\epsilon$ $h^{-1}$kpc | $N_{\Delta t}$ | Code | $r_{\rm conv}$ $h^{-1}$kpc |
|---|---|---|---|---|---|---|---|
| C4 | 1316.7 | 53101.9 | 1050402 | 5.0 | EpsAcc | GADGET | 15.9 |
| C5 | 1375.5 | 60541.8 | 1199299 | 5.0 | EpsAcc | GADGET | 16.2 |
| C6 | 1521.1 | 81870.6 | 1626161 | 5.0 | EpsAcc | GADGET | 15.5 |
| C7 | 1245.8 | 44979.4 | 887837 | 5.0 | EpsAcc | GADGET | 16.4 |
| C8 | 1365.4 | 59220.3 | 1172850 | 5.0 | EpsAcc | GADGET | 16.8 |

TABLE 2

PROPERTIES OF ROTATION CURVES AND FIT PARAMETERS

| Galaxy ID | $r_{\max}$ (kpc) | $V_{\max}$ (km/s) | $V(r_{\mathrm{outer}})$ (km/s) | $r_t$ (kpc) | $\gamma$ | $V_0$ (km/s) | $\chi^2_{\mathrm{red}}$ |
|---|---|---|---|---|---|---|---|
| de Blok et al. (2001b): | | | | | | | |
| ESO0140040 | 21.2 | 272.7 | 262.8 | 3.5 | 1.5 | 272.7 | $5.26 \times 10^{-1}$ |
| ESO0840411 | 8.9 | 61.3 | 61.3 | 10.7 | 1.4 | 105.4 | $2.22 \times 10^{-1}$ |
| ESO1200211 | 3.5 | 25.4 | 25.4 | 1.1 | 5.0 | 22.8 | $4.41 \times 10^{-2}$ |
| ESO1870510 | 2.7 | 39.9 | 39.9 | 1.5 | 1.1 | 55.9 | $2.49 \times 10^{-2}$ |
| ESO2060140 | 11.7 | 118.0 | 118.0 | 1.9 | 1.6 | 123.9 | $9.74 \times 10^{-2}$ |
| ESO3020120 | 10.0 | 86.3 | 86.0 | 3.3 | 2.6 | 88.0 | $2.51 \times 10^{-3}$ |
| ESO3050090 | 4.4 | 54.6 | 54.0 | 3.1 | 1.6 | 71.3 | $5.23 \times 10^{-2}$ |
| ESO4250180 | 14.4 | 144.5 | 144.5 | 5.0 | 1.1 | 177.2 | $9.18 \times 10^{-2}$ |
| ESO4880049 | 6.0 | 97.1 | 97.1 | 2.5 | 1.1 | 128.5 | $6.20 \times 10^{-3}$ |
| F563-1 | 13.4 | 112.4 | 110.9 | 2.2 | 1.1 | 121.8 | $9.97 \times 10^{-2}$ |
| F568-3 | 11.2 | 101.1 | 101.1 | 4.8 | 5.4 | 98.4 | $3.14 \times 10^{-2}$ |
| F571-8 | 14.0 | 143.9 | 143.9 | 2.8 | 0.8 | 196.7 | $6.22 \times 10^{-1}$ |
| F579-v1 | 11.6 | 114.4 | 114.2 | 1.1 | 1.4 | 115.7 | $3.73 \times 10^{-2}$ |
| F583-1 | 14.0 | 86.9 | 86.9 | 4.0 | 2.0 | 91.1 | $9.79 \times 10^{-3}$ |
| F583-4 | 6.7 | 69.9 | 69.9 | 1.2 | 0.6 | 122.2 | $1.67 \times 10^{-1}$ |
| F730-v1 | 11.9 | 145.3 | 145.3 | 2.2 | 1.3 | 157.3 | $7.43 \times 10^{-2}$ |
| UGC11454 | 11.9 | 152.2 | 152.2 | 2.8 | 1.3 | 172.1 | $4.36 \times 10^{-1}$ |
| UGC11557 | 6.2 | 80.4 | 80.4 | 14.1 | 1.0 | 264.3 | $4.61 \times 10^{-2}$ |
| UGC11583 | 1.5 | 35.6 | 35.6 | 0.9 | 4.7 | 35.0 | $3.28 \times 10^{-2}$ |
| UGC11616 | 9.6 | 142.8 | 142.8 | 2.4 | 1.7 | 142.2 | $1.98 \times 10^{-1}$ |
| UGC11648 | 12.7 | 144.6 | 144.6 | 57.5 | -0.2 | 13.0 | $4.72 \times 10^{-1}$ |
| UGC11748 | 5.3 | 250.0 | 246.5 | 2.3 | 10.4 | 235.4 | $1.95 \times 10^{0}$ |
| UGC11819 | 8.9 | 154.7 | 152.6 | 4.6 | 3.3 | 154.7 | $4.22 \times 10^{-1}$ |
| UGC4115 | 1.0 | 39.8 | 39.8 | 2.1 | 1.2 | 115.9 | $2.20 \times 10^{-3}$ |
| UGC5750 | 21.8 | 78.9 | 78.9 | 7.0 | 3.4 | 80.5 | $8.95 \times 10^{-3}$ |
| UGC6614 | 45.4 | 205.2 | 203.9 | 2.8 | 1.2 | 201.9 | $2.30 \times 10^{0}$ |
| de Blok and Bosma (2002): | | | | | | | |
| DDO185 | 2.2 | 49.6 | 49.6 | 2.3 | 1.1 | 76.2 | $1.88 \times 10^{0}$ |
| DDO189 | 6.4 | 65.7 | 64.4 | 1.7 | 1.7 | 68.8 | $5.33 \times 10^{-2}$ |
| DDO47 | 3.2 | 67.0 | 67.0 | 2.9 | 1.7 | 88.0 | $2.75 \times 10^{-1}$ |
| DDO52 | 3.1 | 50.0 | 50.0 | 1.2 | 79.4 | 45.9 | $3.34 \times 10^{0}$ |
| DDO64 | 2.7 | 46.9 | 46.9 | 1.6 | 2.0 | 58.0 | $5.06 \times 10^{-1}$ |
| IC2233 | 7.4 | 92.8 | 92.8 | 5.1 | 1.1 | 135.2 | $1.39 \times 10^{0}$ |
| F563-1 | 17.5 | 114.1 | 114.1 | 2.8 | 1.2 | 123.9 | $2.67 \times 10^{-1}$ |
| NGC100 | 8.0 | 91.3 | 91.3 | 2.6 | 1.8 | 95.0 | $8.90 \times 10^{-2}$ |
| NGC1560 | 7.9 | 77.5 | 77.5 | 1.8 | 1.0 | 94.8 | $8.30 \times 10^{0}$ |
| NGC2366 | 1.4 | 55.5 | 54.6 | 1.5 | 20.1 | 54.2 | $2.41 \times 10^{-1}$ |
| NGC3274 | 2.1 | 82.6 | 79.5 | 0.7 | 1.9 | 81.2 | $7.82 \times 10^{-1}$ |
| NGC4395 | 7.6 | 84.2 | 82.6 | 1.2 | 1.0 | 92.8 | $5.65 \times 10^{-1}$ |

TABLE 2—*Continued*

| Galaxy ID | $r_{\max}$ (kpc) | $V_{\max}$ (km/s) | $V(r_{\mathrm{outer}})$ (km/s) | $r_t$ (kpc) | $\gamma$ | $V_0$ (km/s) | $\chi^2_{\mathrm{red}}$ |
|---|---|---|---|---|---|---|---|
| NGC4455 | 5.9 | 64.4 | 64.4 | 1.8 | 0.9 | 92.7 | $1.96 \times 10^{-1}$ |
| NGC5023 | 5.9 | 84.4 | 84.4 | 1.4 | 1.4 | 95.0 | $2.57 \times 10^{-1}$ |
| UGC10310 | 9.0 | 75.0 | 75.0 | 3.7 | 1.6 | 82.7 | $2.76 \times 10^{-1}$ |
| UGC1230 | 14.1 | 112.7 | 102.9 | 4.3 | 10.6 | 105.1 | $6.43 \times 10^{-2}$ |
| UGC1281 | 5.2 | 56.9 | 56.9 | 3.0 | 5.4 | 57.2 | $7.14 \times 10^{-3}$ |
| UGC3137 | 13.5 | 106.9 | 104.6 | 4.8 | 3.3 | 106.6 | $8.77 \times 10^{-2}$ |
| UGC3371 | 10.3 | 85.7 | 85.7 | 5.6 | 1.7 | 101.9 | $2.76 \times 10^{-3}$ |
| UGC4173 | 12.2 | 57.0 | 57.0 | 5.5 | 0.6 | 119.2 | $9.59 \times 10^{-3}$ |
| UGC4325 | 4.6 | 122.6 | 122.6 | 4.6 | 1.4 | 208.7 | $1.37 \times 10^{-2}$ |
| UGC5005 | 22.0 | 100.0 | 99.1 | 6.6 | 1.2 | 119.9 | $4.75 \times 10^{-2}$ |
| UGC5750 | 5.7 | 49.6 | 49.6 | 6.4 | 3.8 | 63.7 | $1.27 \times 10^{-2}$ |
| UGC711 | 15.4 | 91.6 | 91.6 | 6.8 | 3.1 | 91.8 | $6.55 \times 10^{-2}$ |
| Swaters et al. (2003): | | | | | | | |
| F563V2 | 7.5 | 113.1 | 111.2 | 2.5 | 7.0 | 109.4 | $3.10 \times 10^{-1}$ |
| F5681 | 12.4 | 130.7 | 130.7 | 1.4 | 1.3 | 133.6 | $3.49 \times 10^{0}$ |
| F5683 | 5.6 | 111.2 | 100.6 | 5.1 | 52.2 | 96.6 | $1.85 \times 10^{0}$ |
| F568V1 | 8.9 | 124.9 | 118.2 | 2.5 | 1.7 | 121.9 | $7.99 \times 10^{-1}$ |
| F5741 | 11.5 | 104.2 | 102.6 | 2.4 | 1.3 | 112.2 | $5.58 \times 10^{-1}$ |
| UGC11557 | 10.4 | 84.5 | 84.5 | 6.0 | 0.7 | 189.7 | $6.27 \times 10^{-1}$ |
| UGC11707 | 15.0 | 99.9 | 99.9 | 1.5 | 0.6 | 149.6 | $3.94 \times 10^{-1}$ |
| UGC11861 | 8.1 | 164.0 | 152.6 | 3.3 | 0.9 | 200.0 | $4.61 \times 10^{0}$ |
| UGC2732 | 15.4 | 98.0 | 98.0 | 1.7 | 0.7 | 127.6 | $6.89 \times 10^{-1}$ |
| UGC2259 | 1.7 | 93.7 | 90.0 | 0.7 | 1.5 | 88.5 | $1.83 \times 10^{0}$ |
| UGC4325 | 2.8 | 104.6 | 91.5 | 1.8 | 3.7 | 93.5 | $8.31 \times 10^{-1}$ |
| UGC4499 | 8.5 | 74.3 | 74.3 | 3.4 | 3.7 | 73.9 | $1.13 \times 10^{0}$ |
| UGC5721 | 2.2 | 80.4 | 78.7 | 0.4 | 1.0 | 86.0 | $7.28 \times 10^{-1}$ |
| UGC731 | 5.8 | 74.0 | 73.9 | 1.3 | 1.4 | 78.7 | $9.74 \times 10^{-1}$ |
| UGC8490 | 6.1 | 80.1 | 77.6 | 1.2 | 2.7 | 79.4 | $5.56 \times 10^{-1}$ |
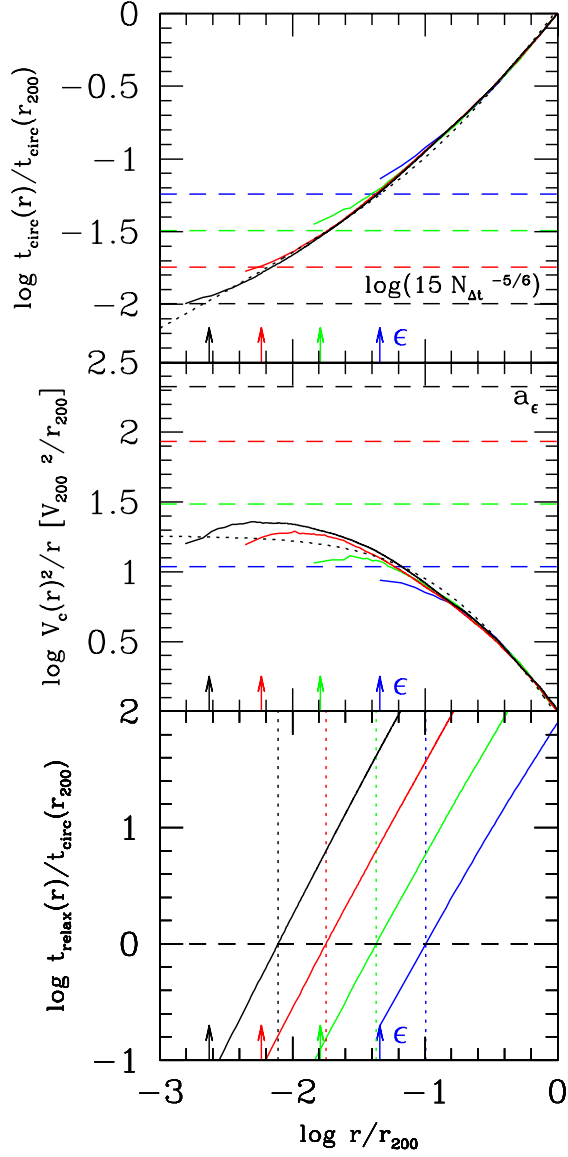
Fig. 1.— The structure of halo G3 at different mass, time, and spatial resolutions. The value of the softening parameter $\epsilon$ is indicated by arrows in the three panels. The number of timesteps and particles are listed in Table 1. Runs with $32^3$, $64^3$, $128^3$ and $256^3$ high-resolution particles are shown in blue, green, red, and black, respectively. Dotted curves show an NFW profile with concentration $c = 5.3$ and $r_{200} = 143.4\ h^{-1}$kpc. *Upper panel:* Circular orbital timescale $t_{\rm circ}$ versus radius; radii at which the circular orbital timescale is less than $15\ N_{\Delta t}^{-5/6}$, indicated by the dashed lines for each simulation, are unresolved due to insufficient time resolution. *Middle panel:* Mean radial acceleration profile $V_c(r)^2/r$; untrustworthy radii are those corresponding to accelerations greater than the limiting acceleration imposed by the softening $a_\epsilon \simeq 0.5\ V_{200}^2/\epsilon$, shown by the dashed lines. *Lower panel:* Collisional relaxation time $t_{\rm relax}$ versus radius; convergence requires $t_{\rm relax} \gtrsim t_{\rm circ}(r_{200})$. Vertical dotted lines indicate the radius, $r_{\rm conv}$, beyond which this condition (the strictest of the three) is satisfied.

20
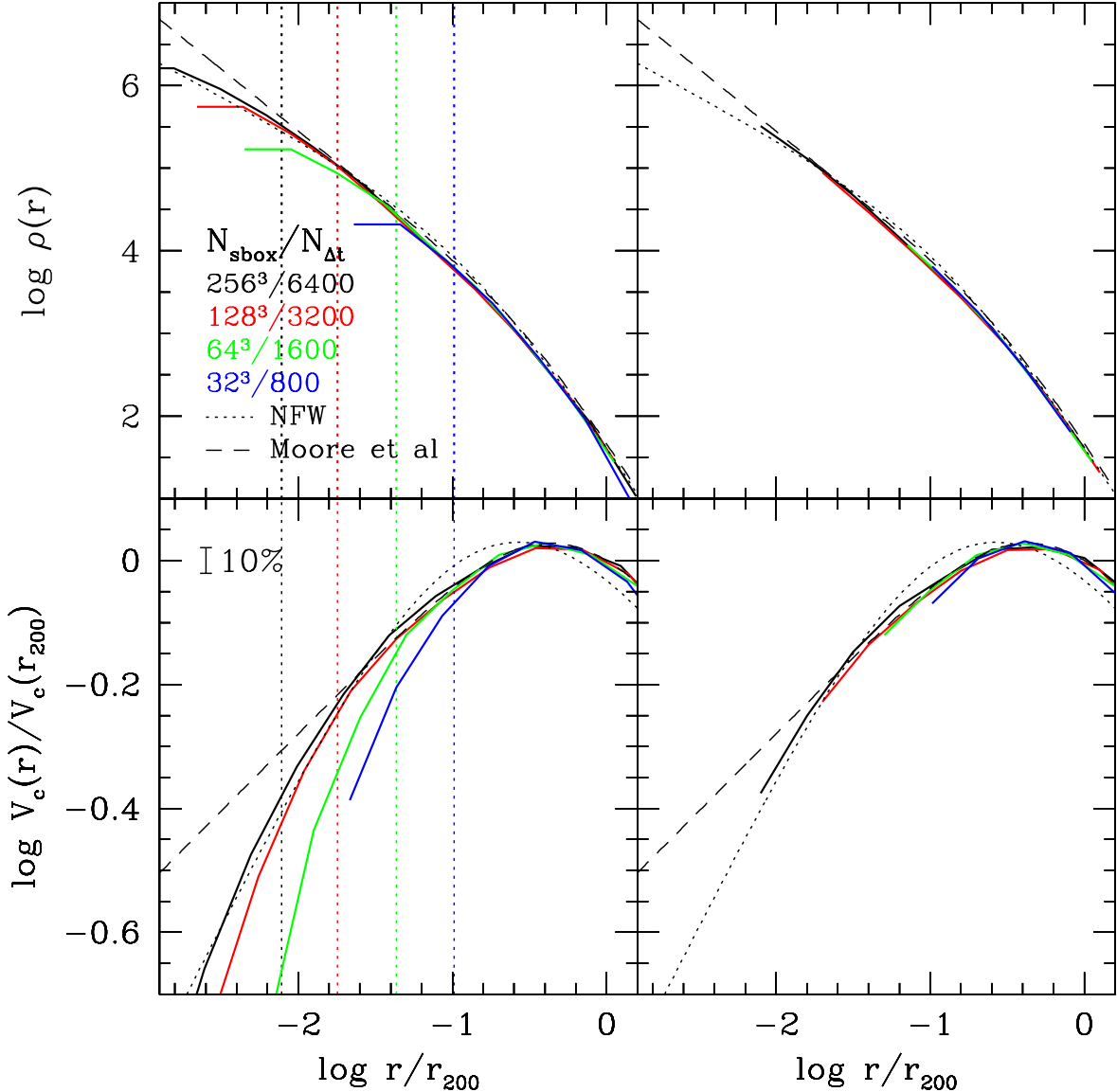
Fig. 2.— *Upper left panel:* Density profiles of halo G3 at four different levels of mass resolution, plotted down to radii containing 50 particles. Dashed and dotted curves show best fit Moore et al. and NFW profiles, respectively (see text for fitting details). Vertical dotted lines indicate the minimum converged radius, $r_{conv}$, for each run. *Upper right panel:* Same density profiles plotted only for converged radii. The discrepancy between lower resolution runs and the highest resolution simulation at small radii is no longer apparent when only reliably resolved radii are considered. Lower panels are as the upper ones, but for the circular velocity profiles.
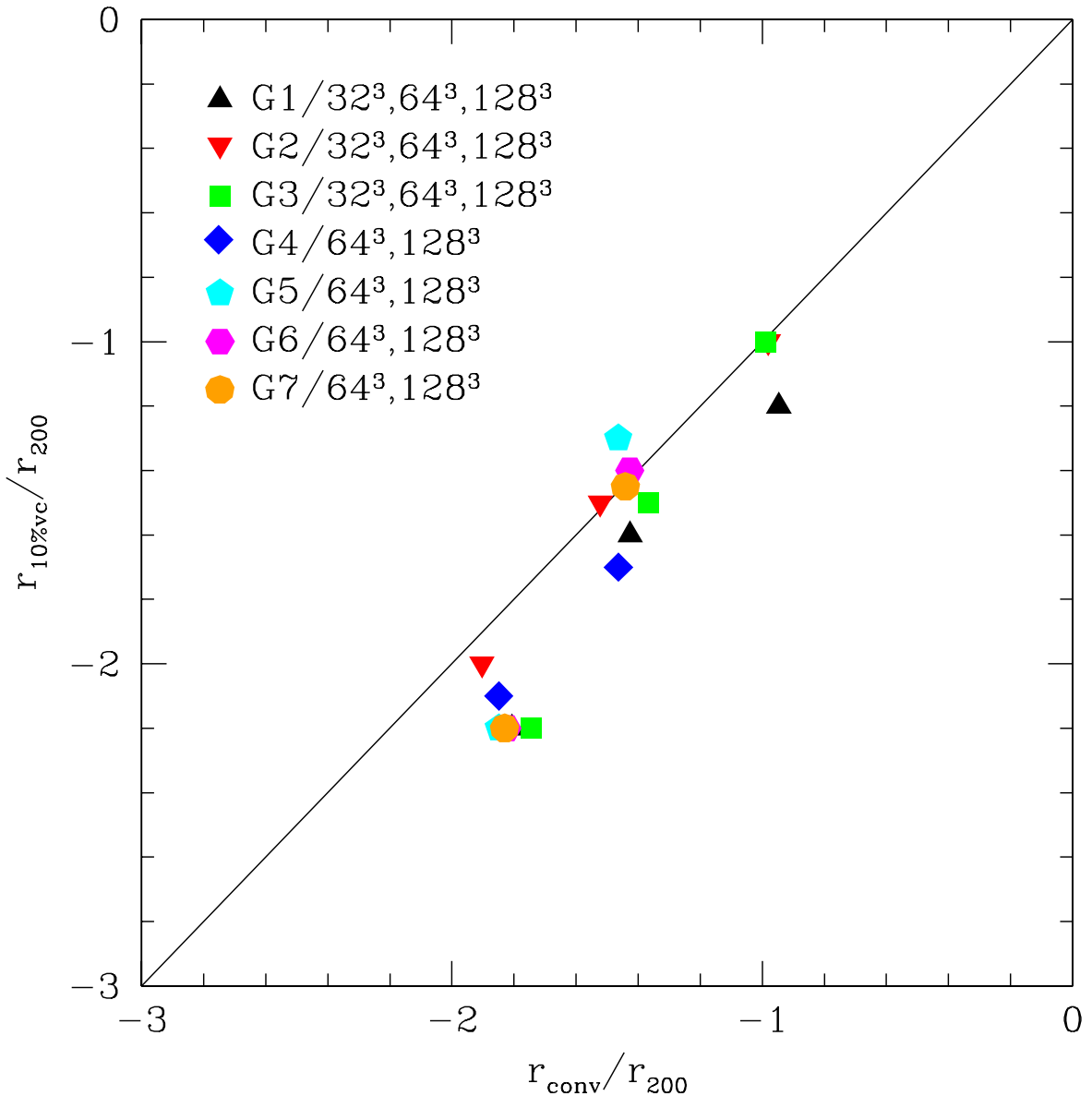
Fig. 3.— Radius where the circular velocity profile of lower resolutions runs starts to deviate from that of the highest resolution run by more than 10%, $r_{10\%vc}$, plotted against the minimum converged radius predicted by the P03 convergence criteria, $r_{\rm conv}$. In all cases $r_{\rm conv} \leq r_{10\%vc}$, validating the P03 criteria as conservative estimators of the converged region.
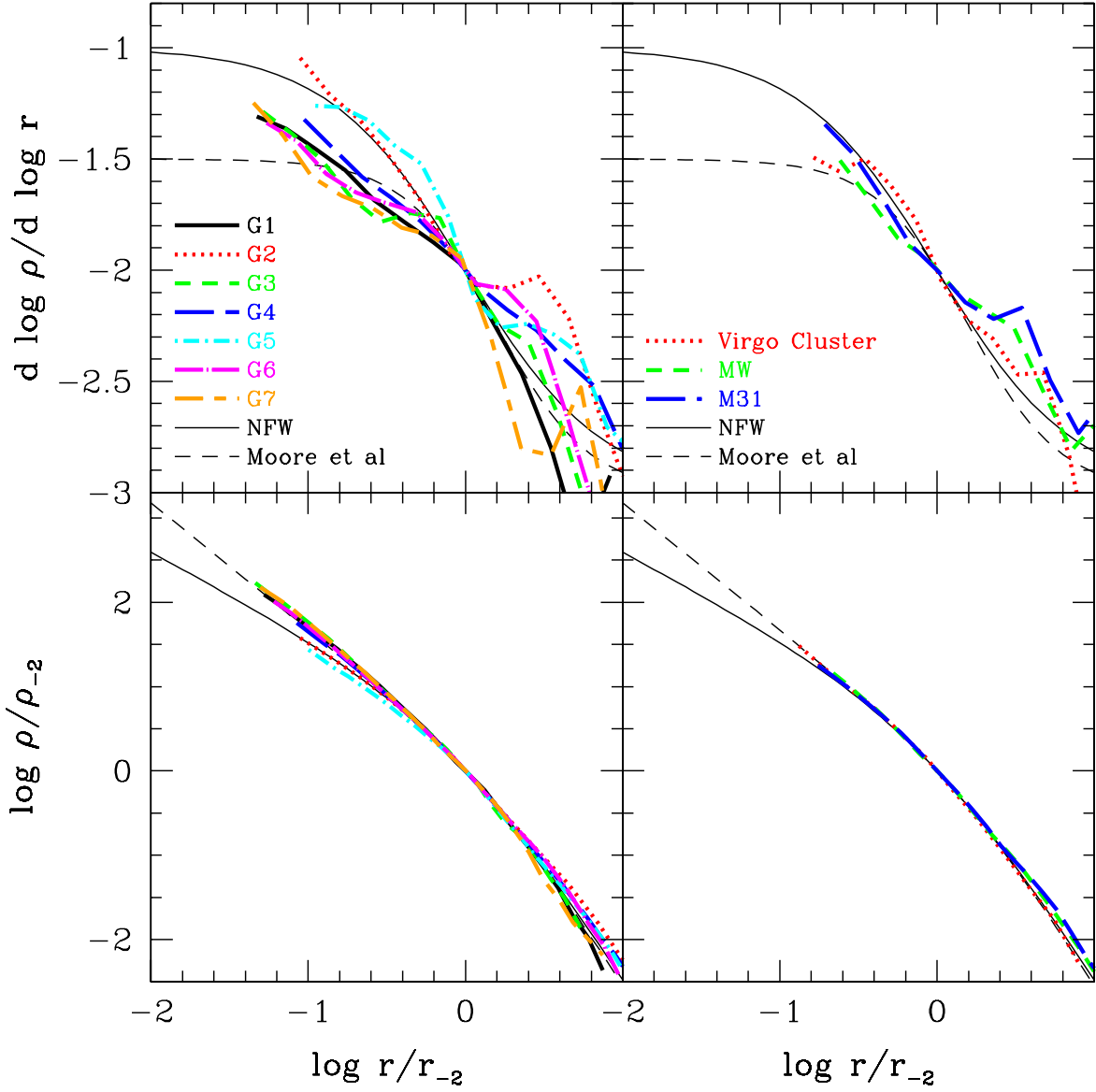
Fig. 4.— *Upper left panel:* Logarithmic slope of the smoothed density profile of halos simulated at our highest resolution $N_{\rm sbox} = 256^3$, plotted for $r \geq r_{\rm conv}$. Curves are scaled horizontally to the radius $r_{-2}$, where the slope takes the isothermal value, $d \log \rho / d \log r(r_{-2}) = -2$. NFW and Moore et al. profiles are shown as solid and dashed curves, respectively. The logarithmic slope increases monotonically with decreasing radius and there is no obvious convergence to a particular asymptotic value of the central slope. *Upper right panel:* Same as upper-left but for the SCDM Virgo cluster of Ghigna et al. (2000) and SCDM Milky Way (MW) and M31 galaxy halos of Moore et al. (1999). The profiles of the two galaxy-sized halos appear to be consistent with those of our halos. The logarithmic slope of the cluster halo appears to be slightly steeper than the others, fluctuating about a value of $-1.4$ at the innermost resolved point. *Lower left panel:* Halo density profiles scaled horizontally to radius $r_{-2}$ and vertically to the corresponding density at that radius $\rho_{-2} \equiv \rho(r_{-2})$. *Lower right Panel:* Same as lower-left but for the Ghigna et al. (2000) and Moore et al. (1999) halos.
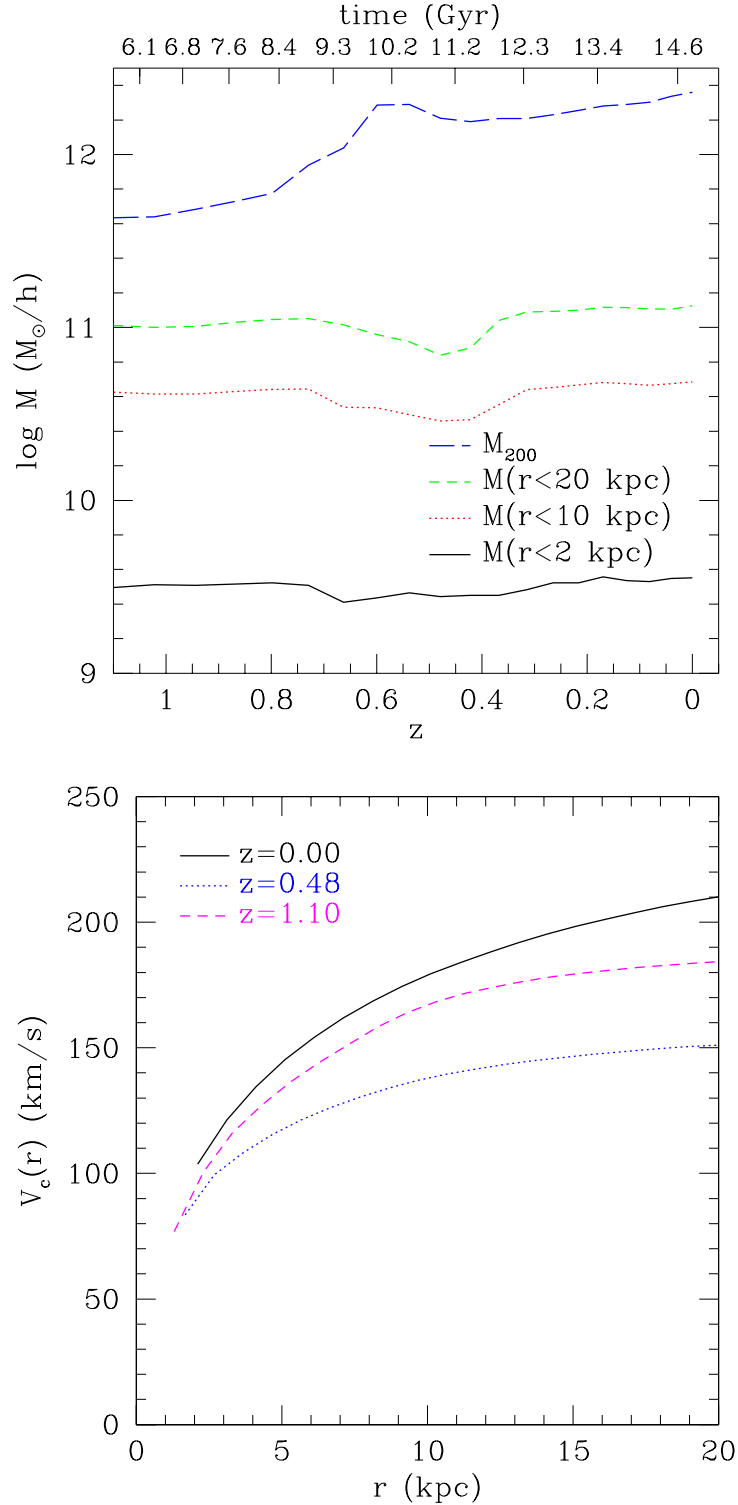
Fig. 5.— *Top panel:* Mass within $r = 2$, 10, and 20 kpc (physical) and $r_{200}$ for halo G1/256$^3$ as a function of redshift (age of Universe in Gyr) on bottom (top) axis. The mass within 20 kpc undergoes significant fluctuations in response to a merger at $z \simeq 0.7$. *Bottom panel:* The inner circular velocity profile before ($z = 1.10$), during ($z = 0.48$), and after ($z = 0$) the merger. The shape of the $V_c$ profile is noticeably altered by the effects of the infalling substructure.

24
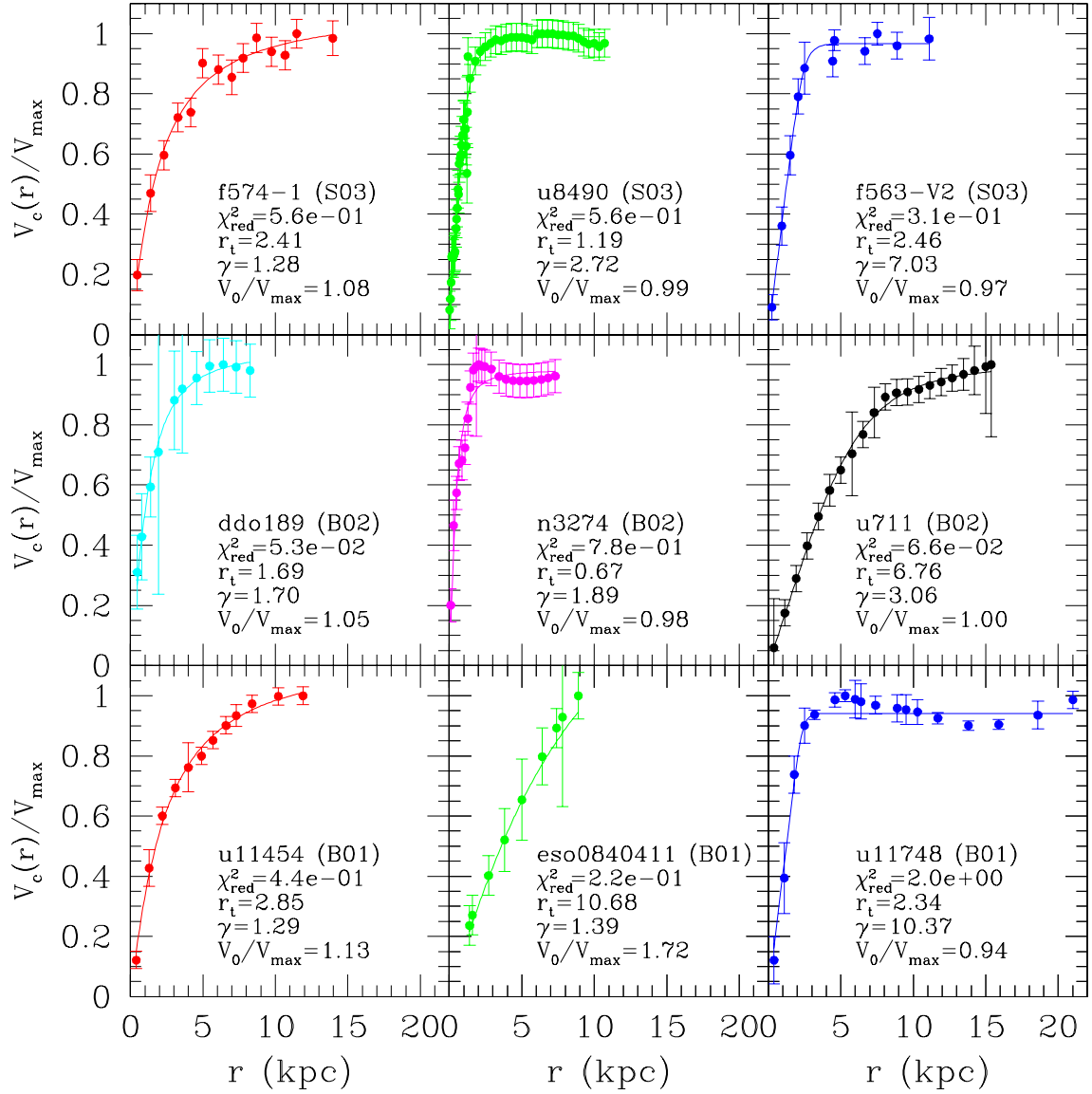
Fig. 6.— LSB rotation curves from the datasets of de Blok et al. (2001b) (B01), de Blok and Bosma (2002) (B02) and Swaters et al. (2003) (S03). Solid curves show best fits using the Courteau (1997) fitting formula given by eq. 7. Best fits with $\gamma \sim 1$ correspond to rotation curves that rise and turn over gently as a function of radius. Curves with $\gamma > 2$ feature a much sharper transition from the rising to the flat part of the curve. See text for full discussion.
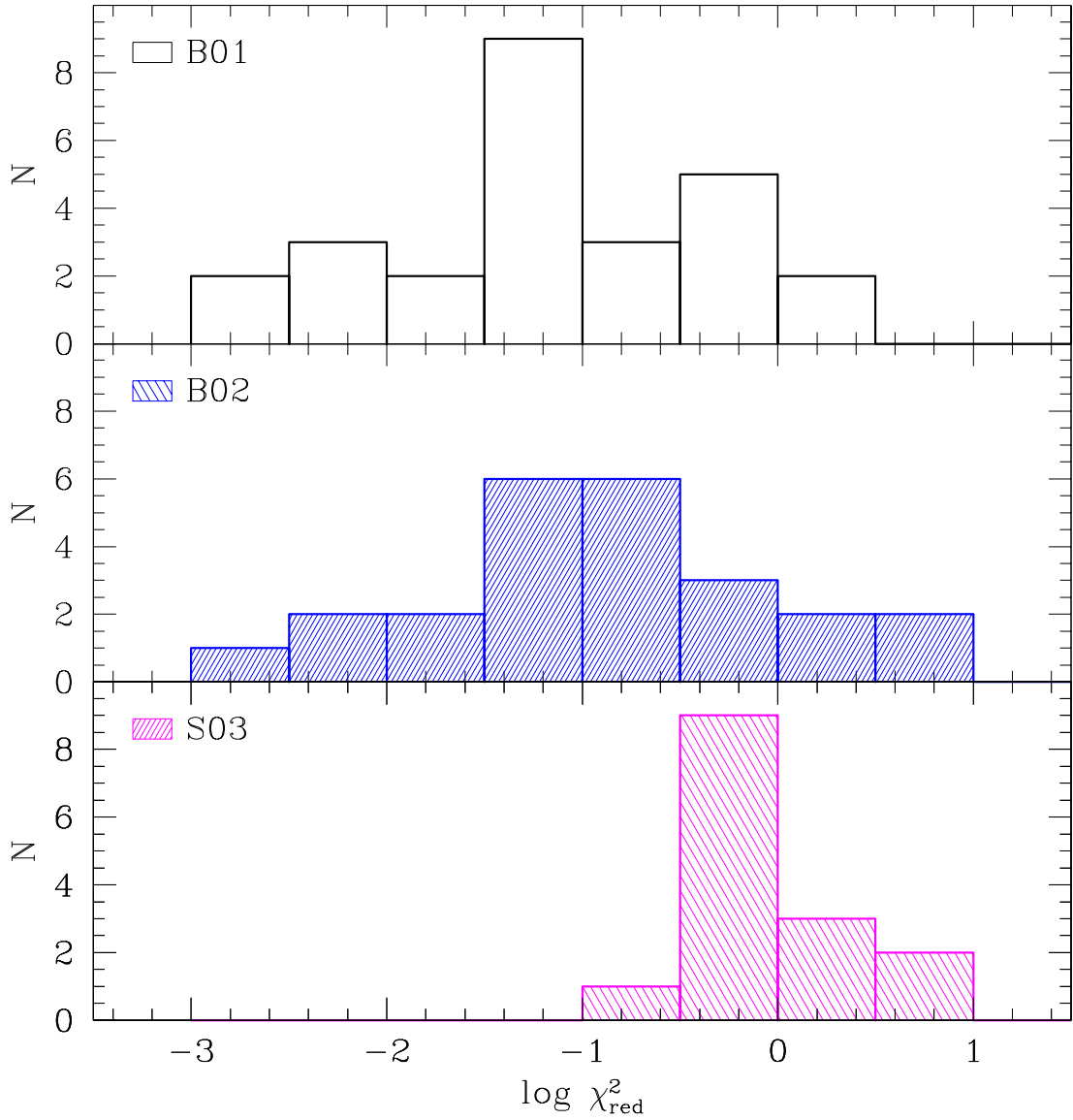
Fig. 7.— Distribution of reduced $\chi^2$ values corresponding to best fits using the multi-parameter fitting formula given by eq. 7 for the three rotation curve datasets (B01, B02, S03). Note that the B01 and B02 $\chi^2_{\rm red}$ distributions peak at unrealistically low values, signalling the presence of significant correlation between neighbouring points in the rotation curves of these samples. The S03 $\chi^2$ distribution peaks at a higher value, emphasizing the various assumptions of different authors when deriving rotation curves from raw data (see also Figure 8).
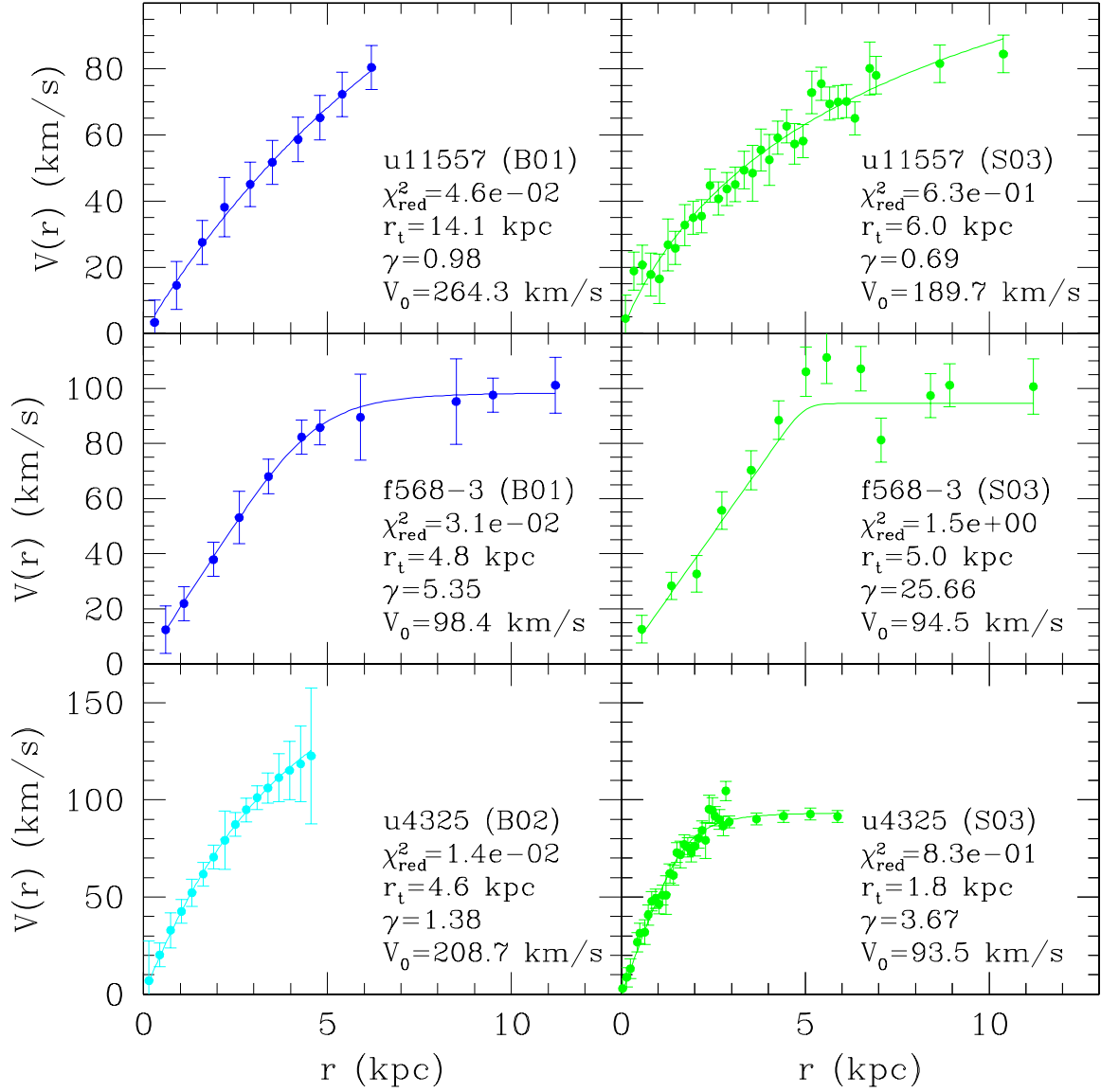
Fig. 8.— Rotation curves of UGC 11557, F568-3, and UGC 4325 derived by either de Blok et al. (2001b); de Blok and Bosma (2002) (B01 and B02, left panels) or Swaters et al. (2003) (S03, right panels). Solid curves show fits to the rotation curves using eq. 7. Values of the three fitting parameters $\gamma$, $r_t$, and $V_0$ are listed in each panel along with the corresponding reduced chi-squared, $\chi^2_{\mathrm{red}}$. This figure illustrates the effect on the derived rotation curves due to different assumptions and methodology adopted by various authors. In the case of UGC 4325, for example, the rotation curve derived by B02 continues to rise out to the last measured point at $V \simeq 120 \ \mathrm{km \, s^{-1}}$, whereas the the S03 curve flattens off at $V \simeq 90 \ \mathrm{km \, s^{-1}}$.
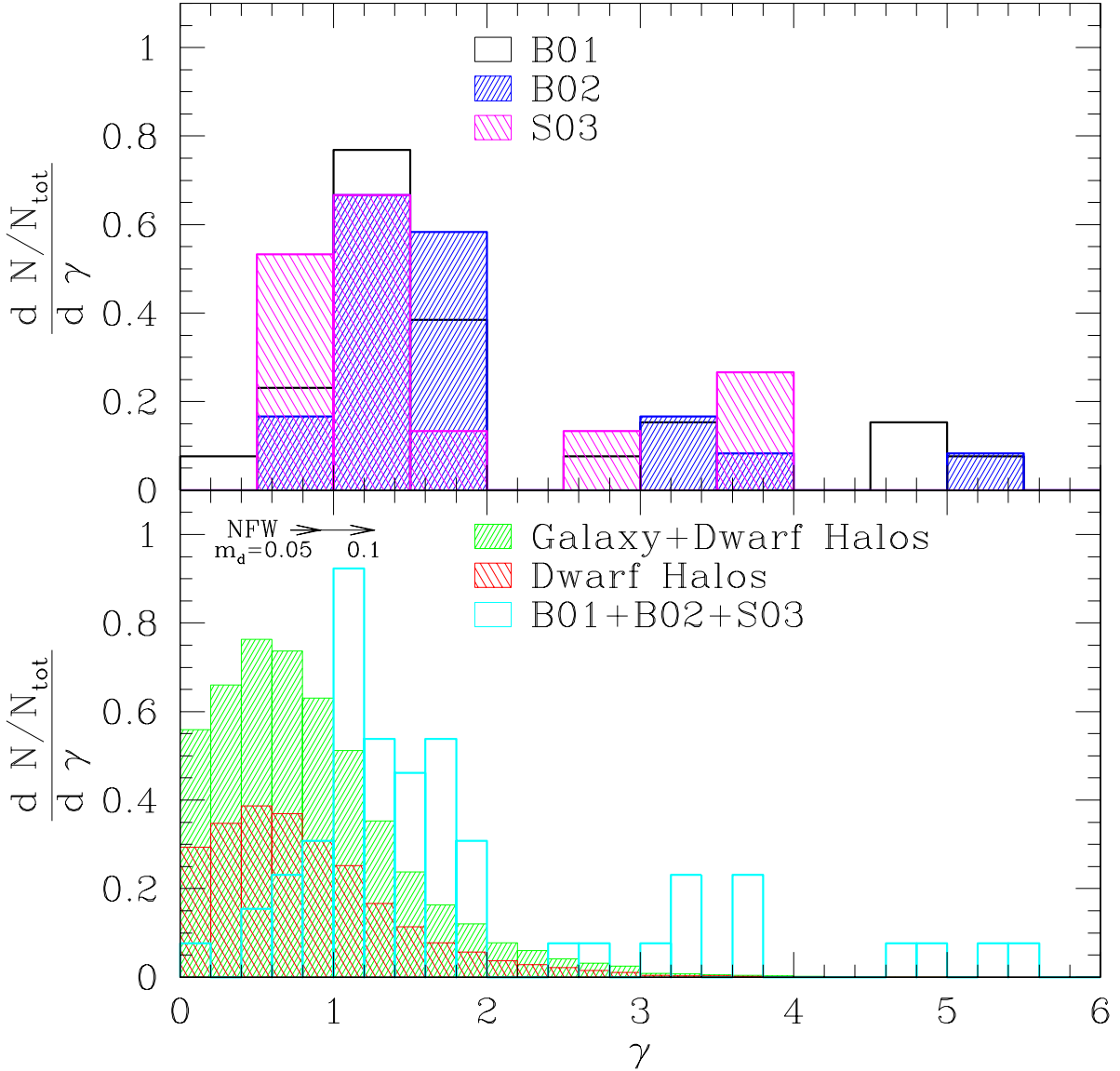
Fig. 9.— *Top panel:* Distribution of best-fit $\gamma$ values obtained for galaxies in the samples of de Blok et al. (2001b) (B01), de Blok and Bosma (2002) (B02), and Swaters et al. (2003) (S03). Note that most galaxies in all three samples cluster around $\gamma = 1.2$, but that there are a significant number of outliers with $\gamma \gtrsim 2.5$. These define a population of galaxies that seems to be distinct from the bulk of the sample. *Bottom panel:* Combined observational sample compared with the halo $\gamma$ distribution after convolution with an error distribution similar to that corresponding to observed rotation curve fits. Arrows show the change in $\gamma$ caused by the addition of an exponential disk to an NFW halo with concentration $c = 10$. The mass of the disk, $m_d$, is given in units of the halo mass. Its exponential scale length is computed assuming that the spin parameter of the halo is $\lambda = 0.1$, and that the specific angular momentum of the disk is the same as that of the halo (Mo et al. 1998). The magnitude of the correction (shown by horizontal arrows) suggests that the $\gamma$ distribution of halos might actually be consistent with that of the bulk of galaxies, but apparently fails to account for the $\gamma \gtrsim 2.5$ tail in the rotation curve distribution. See text for further details.
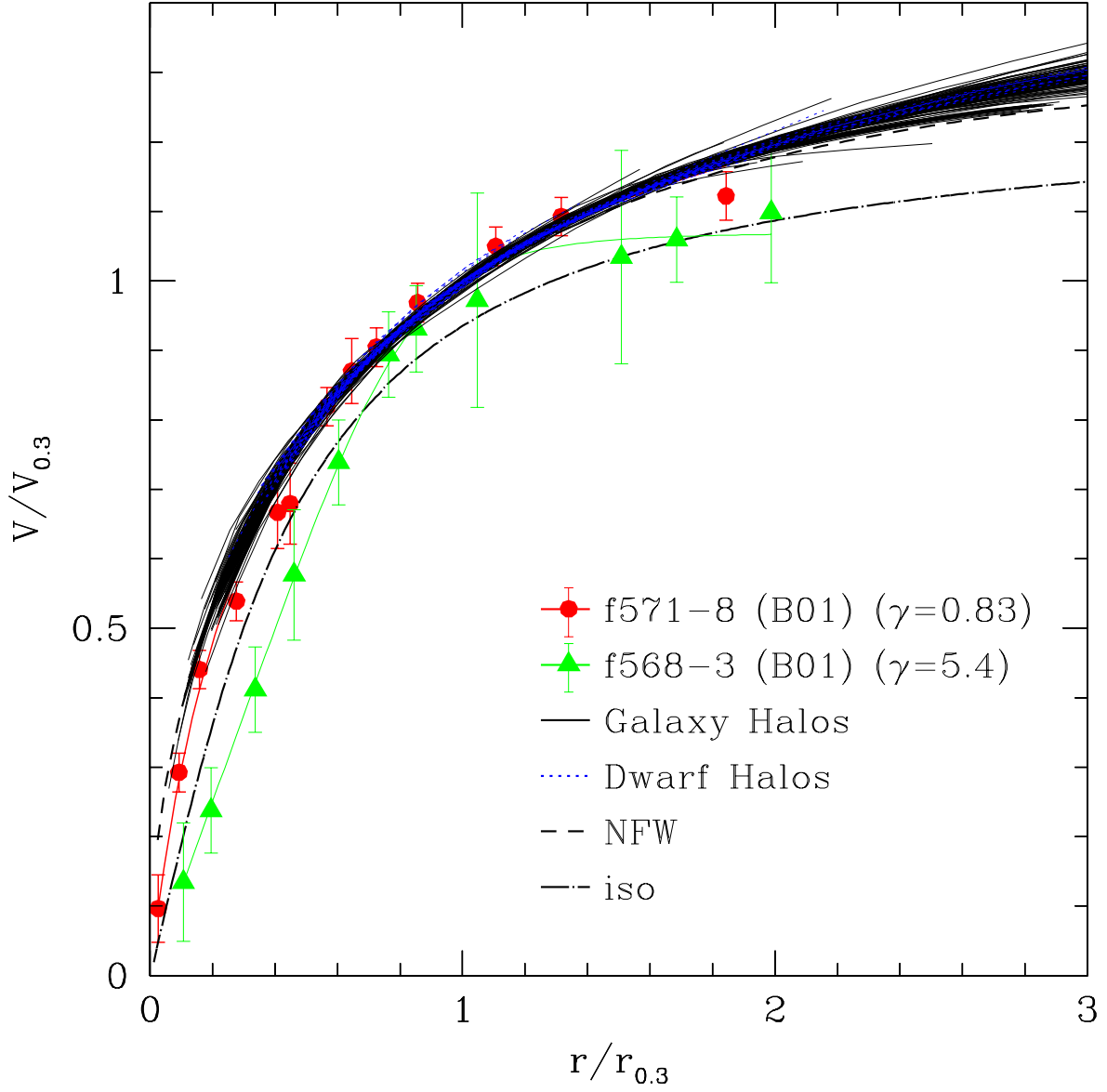
Fig. 10.— Rotation curves of two galaxies, one with $\gamma = 0.83$ (f571-8, filled circles), representative of the bulk of the population, and another one with $\gamma = 5.4$ (f568-3, filled triangles) representative of the tail of the distribution. The curves have been scaled to the radius, $r_{0.3}$, (and corresponding velocity, $V_{0.3}$) where the logarithmic slope of the fit to the rotation curve is $d \log V / d \log r = 0.3$. Galaxy (dwarf) halos are shown by solid (dotted) lines, and they appear to follow closely the NFW profile (dashed line). This figure shows clearly that halo $V_c$ profiles are inconsistent with rotation curves with high $\gamma$, such as f568-3. The dot-dashed curve shows that f568-3 is somewhat better matched by a non-singular isothermal sphere model.
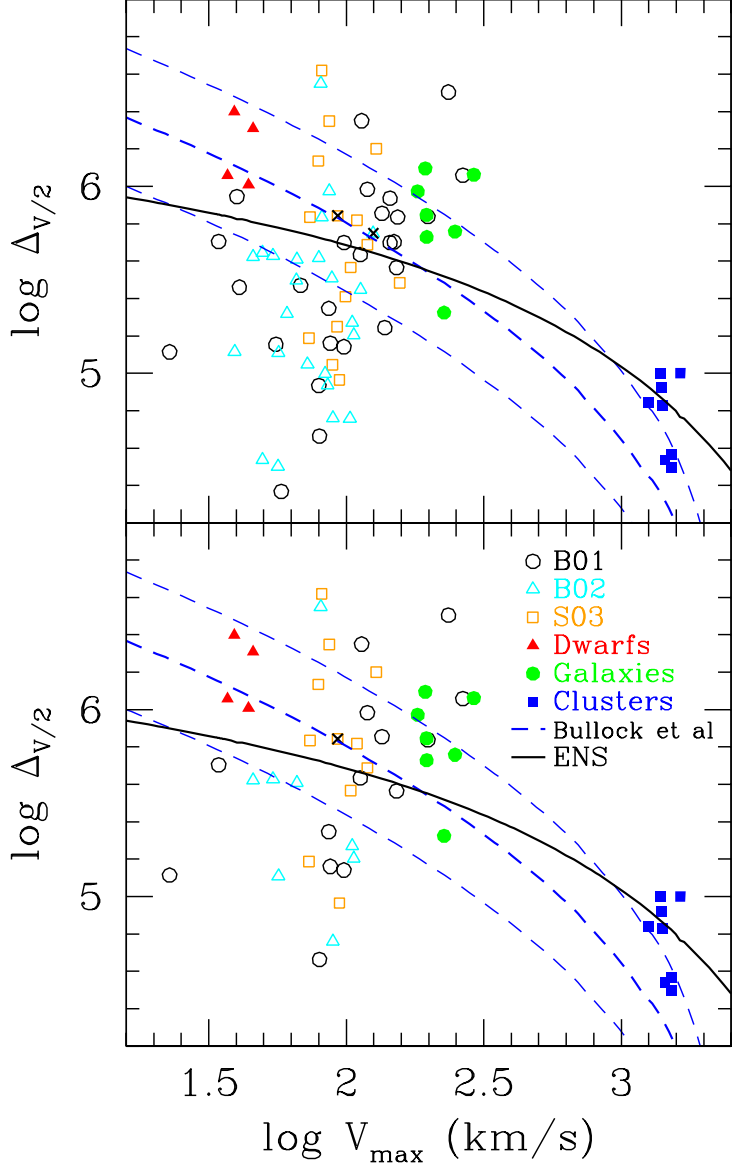
Fig. 11.— Alam et al. (2002) halo concentration parameter, $\Delta_{V/2}$, inferred from rotation curves of LSB galaxies in the B01, B02, and S03 samples (open symbols), compared to those measured for simulated dwarf- ($\log V_{\max} \simeq 1.6$), galaxy- ($\log V_{\max} \simeq 2.3$), and cluster-sized ($\log V_{\max} \simeq 3.2$) halos (solid symbols). Points corresponding to $\Delta_{V/2}$ values for UGC 4325 calculated from B01 and S03 rotation curves are marked with an ×. Solid line shows the prediction of the Eke et al. (2001) concentration model for NFW halos in a $\Lambda$CDM cosmogony ($\Omega_0 = 0.3$, $\Omega_\Lambda = 0.7$, and $h = 0.65$, $\sigma_8 = 0.9$). Dashed lines show the prediction (and $1\,\sigma$ scatter) corresponding to the Bullock et al. (2001) concentration model. *Top panel:* All galaxies in combined B01, B02, and S03 dataset. *Bottom panel:* Only galaxies whose rotation curves are not rising steeply at the outermost point ($d \log V/d \log r(r_{\rm outer}) < 0.1$).